INTERNATIONAL JOURNAL FOR NUMERICAL METHODS IN ENGINEERING
Int. J. Numer. Meth. Engng 2007; **71**:931–962
Published online 5 January 2007 in Wiley InterScience (www.interscience.wiley.com). DOI: 10.1002/nme.1970

A contact mechanics model for quasi-continua

Roger A. Sauer and Shaofan Li*, †

Department of Civil and Environmental Engineering, University of California, Berkeley, CA 94720, U.S.A.

SUMMARY

A computational multiscale contact mechanics model is proposed to describe the interaction between deformable solids based on the interaction of individual atoms or molecules belonging to the solids. The contact model, formulated in the framework of large deformation continuum mechanics, is derived from coarsening the molecular dynamics (MD) description of a large assembly of individual atoms, and it thus bears some of the characteristics of the underlying atomic structure. The multiscale contact model distinguishes between atoms interacting within a small neighbourhood within the solids and atoms interacting over large distances between remote regions of the solids. The former furnishes a constitutive relation for the continuum, like the Cauchy–Born Rule, while the latter is used to model the interaction between distinct bodies. The proposed contact model is formulated as a variational weak form and implemented within an updated Lagrangian finite element method. It is shown that, as the problem size increases, the description of the model can be simplified to yield more efficient computational algorithms. In this respect, the proposed multiscale formulation leads to a smooth transition from MD to continuum contact mechanics. The general behaviour of the contact model is studied, and some numerical examples are given. Copyright © 2007 John Wiley & Sons, Ltd.

Received 11 March 2006; Revised 15 November 2006; Accepted 17 November 2006

KEY WORDS: coarse-graining; contact; finite element method; nano-mechanics; quasi-continuum

1. INTRODUCTION

Much attention has been devoted to the contact description of large-scale objects, either analytically, [1] or computationally, [2, 3]. On the other hand, with the emergence of nanotechnology, the nanoscale treatment of contact and related subjects such as adhesion, indentation and tribology are becoming more prominent. In macroscopic contact modelling, the contact behaviour of two interacting bodies is governed by the principles of continuum mechanics and the unilateral constraint

*Correspondence to: Shaofan Li, Department of Civil and Environmental Engineering, University of California, Berkeley, CA 94720, U.S.A.
†E-mail: li@ce.berkeley.edu

Contract/grant sponsor: NSF; contract/grant number: CMS-0239130

that the bodies may not penetrate each other. As the problem size decreases to the nanoscale, the contact interaction between two small objects may not be appropriately described by macroscale contact mechanics, due to the emergence of atomic effects.

Contact interaction at atomic or sub-atomic scales can be simulated by first-principle methods such as molecular dynamics (MD) e.g. [4]. This is the predominant case in the study of interactions among flexible nanotubes [5, 6], DNA strands and proteins [7], nanoindentation [8–10], and atomic force microscopy [11, 12]. However, most of these simulations are qualitative in nature and focus on general scientific principles rather than the quantitative engineering design in nanotechnology. Even in the near future, it may not be practical to use first principle-based simulations to model such systems in engineering design, due to the computational expense, complexity, and difficulties in interpreting results. Small-scale contact phenomena can be efficiently modelled by the analytical theories of Johnson, Kendall and Roberts (JKR) [13], of Derjaguin, Muller and Toporov (DMT) [14], and by the related Maugis–Dugdale model [15]. These analytical mesoscale contact models have shown close agreement with experimental results, and have been successfully applied to some engineering and biology problems. Despite their success, these models are restricted to infinitesimal deformations and simple geometry of the interacting bodies.

In this work, we present a computational quasi-continuum contact mechanics model, formulated for arbitrarily shaped nanoscale solids undergoing large deformation, whose interaction is based on the interaction of individual atoms. In recent years, the atomistic potential-based *quasi-continuum model* developed by Tadmor *et al.* [16], see also Knap and Ortiz [17], has been used successfully in multiscale modelling. Nevertheless, it seems to us that a systematic treatment on the contact mechanics of a quasi-continuum is still lacking. The key to build a nanoscale contact model within a quasi-continuum framework is the homogenization of the long-range atomic interaction to obtain the effective interaction between continua. To capture this effective interaction, we propose three different computational strategies, which form a seamless transition from MD to macroscale computational contact mechanics: at large scales two bodies interact *via* tractions acting on their contacting surfaces, whereas at very small scales the interaction expresses itself as a body force field extending over large parts of the interacting bodies. With the proposed three methods, we have successfully formulated and implemented a quasi-continuum contact mechanics model within the framework of the finite element method [18, 19]. The model, termed the *coarse-grained contact model* (CGCM), is computationally more efficient than MD simulations, while, at the same time, is capable of predicting some effects of atomic interactions under finite deformations.

The next section serves as an introduction and idealization of the proposed contact model. It is followed by Section 3, which provides a detailed derivation of the theory of the model. The finite element implementation of the model is discussed in Section 4. The general behaviour of the model and some numerical examples are presented in Section 5. We conclude the presentation in Section 6.

2. A QUASI-CONTINUUM APPROACH TO CONTACT

We proceed by presenting a conceptual overview of the CGC model. Figure 1 illustrates how the model fits into the approaches of classical continuum contact mechanics and MD. At large scales the interaction between two bodies is described by a continuum approach. The bodies under study are considered to be continuous media, whose loading–deformation relation is modelled upon some constitutive relations. In the case of hyperelasticity, the material response derives from a

DOI: 10.1002/nme

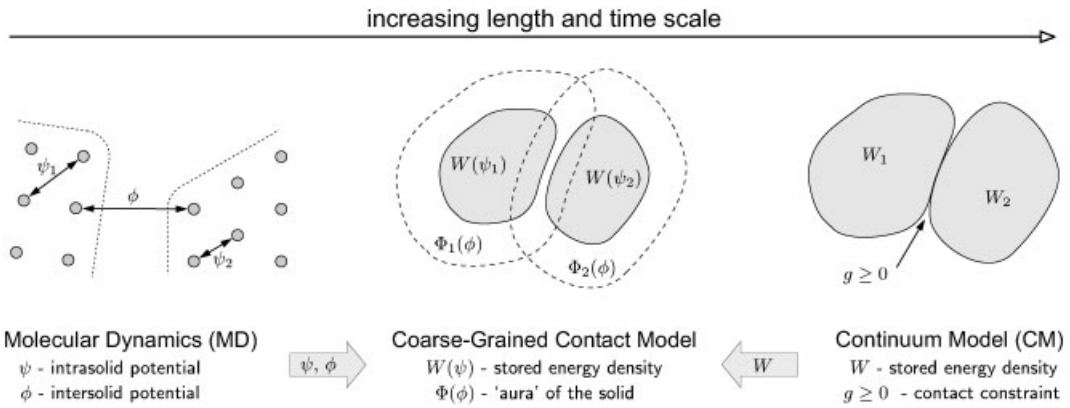

Figure 1. Coarse-grained contact mechanics model (CGCM).

stored energy function W, which can be considered a property of the continuum. The contact of two such bodies is usually modelled as a globally constrained problem, where the constraint is the impenetrability of the two bodies. In other words the gap g between the two bodies must remain positive. Analytical and numerical aspects of continuum contact mechanics can be found in [1–3].

On the other hand, the behaviour at the atomic scale is governed by interactions among individual atoms, which are modelled by interatomic potentials (see Figure 1). Conceptually, we distinguish between two such potentials: the interaction potential ϕ, acting between atoms of two distinct bodies and therefore also termed the *intersolid* potential, and the interaction potential ψ, governing atoms within the solid and thus termed the *intrasolid* potential. This notation is in analogy to the behaviour of carbon nanotubes (CNTs), where we distinguish between the interlayer and intralayer response, e.g. see the review by Qian *et al.* [20]. Molecular dynamics provides a powerful tool to simulate the behaviour of large assemblies of atoms (or molecules), modelled by point masses and atomic interaction potentials. Comprehensive background information on interatomic forces is provided by Israelachvili [21], an introduction into MD can be found in [4]. We note, that a single cubic millimeter can contain more than a billion billion (10^{18}) atoms and that the time scale of atomic oscillations is of the order of picoseconds (10^{-12} s). Thus, it quickly becomes impossible to solve such systems even with state-of-the-art computing technology. Furthermore, for many practical applications, the detailed knowledge of the positions and velocities of all these atoms over time, is of little interest.

A great ambition of multiscale modelling is the concurrent simulation combining both the character of a continuum with the character of a discrete lattice. That is, one seeks to develop a model capable of seamlessly transcending from one scale to the other. The proposed quasi-continuum contact model CGCM combines features from both the continuum and the molecular approach (see Figure 1). From the continuum model 'above' we take the general continuum description of the bodies under consideration. In particular, we use a hyperelastic material model described by an internal potential W. From the molecular approach 'below' we take the short-range interaction potential ψ, to generate the stored energy function W, and we take the long-range interaction potential ϕ and use it to model the interaction between the bodies. In other words ψ furnishes a constitutive relation for the solids, $W = W(\psi)$, whereas ϕ generates an external potential

DOI: 10.1002/nme

field, denoted as $\Phi = \Phi(\phi)$, enveloping the solids like an 'aura'. Physically, the intrasolid interaction can be associated with covalent, ionic, and metallic bonds, which are strong but only act over a close range. An example for the intersolid interaction is the van der Waals attraction between solids, which is relatively weak but of much longer range.

Thus, the essence of the CGCM is an atomic potential-enriched hyperelastic continuum with a surrounding long-range field, which affects the interaction, like adhesion and contact, among different solids. We stress that this continuum model is based on two distinct components: the generation of an internal potential W from ψ, and the generation of an enveloping field Φ based on ϕ. The former has been studied extensively by the original quasi-continuum method, e.g. [16, 22], and we will, for this reason, focus more of our attention on the latter ingredient. The treatment of this second component has a long history in the calculation of continuum van der Waals forces, [21, 23, 24]. However, to the best of our knowledge, the combination of both components into a single model, its formulation within the setting of large deformation continuum contact mechanics, its implementation into a suitable numerical approach, like the finite element method, and the investigation of its general behaviour, have not been studied before.

It is further noted, that for some applications [25, 26], the internal response W can also be taken from an empirical, not atomistic, constitutive approach [27]. In this fashion it becomes apparent that the CGC Model approaches the traditional continuum model for increasing scales, i.e. as the 'aura' Φ vanishes to be replaced by the contact constraint. It is because of this, that the model takes two minor variations: the molecular motivated model, where both the internal response and the enveloping field are based on the quasi-continuum treatment of the atomic behaviour, and the continuum motivated model, where both W and Φ are motivated form the usual continuum modelling. The motivation of our contact model from both these directions is discussed in the following section.

3. THEORY OF THE COARSE-GRAINED CONTACT MODEL

In this section, the weak formulation of the CGCM discussed above is derived. We start by showing that our model can be motivated from coarsening the underlying MD formulation.

3.1. Coarse-graining: forming the mesoscale Lagrangian

Consider the current configurations $\hat{\Omega}_1$ and $\hat{\Omega}_2$ of two bodies consisting of discrete atoms or molecules (see Figure 1). The bodies are *not* continua and we use the hat on $\hat{\Omega}_1$ and $\hat{\Omega}_2$ to indicate this. The location of all atoms within $\hat{\Omega}_1$ is described by the position $\mathbf{z}_i \in \hat{\Omega}_1$ for $i \in \mathscr{I}_1$, where $\mathscr{I}_1$ is the set of n_1 subscripts denoting the n_1 number of atoms within body 1. Further, $\mathbf{z}_j \in \hat{\Omega}_2$, with $j \in \mathscr{I}_2$, describes the position of the n_2 atoms within body 2. For such a discrete assembly of atoms, the potential energy is given by

$$\hat{\Pi}(\mathscr{Z}) = \hat{\Pi}_{\text{int}}(\mathscr{Z}) - \hat{\Pi}_{\text{ext}}(\mathscr{Z}) \tag{1}$$

where the hat is used to emphasize that this is the energy of a discrete system and where $\mathscr{Z} = \{\mathbf{z}_i, \mathbf{z}_j\}$ is the collection of all $n_1 + n_2$ atomic positions.

In principle, each atom interacts with all other atoms. In this derivation we only consider pairwise interaction between atoms and disregard interactions involving three or more atoms. We further

DOI: 10.1002/nme

assume the additivity of the interactions. Then the internal energy can be written as

$$\hat{\Pi}_{\text{int}}(\mathscr{Z}) = \sum_{k=1}^{b_1} \psi_1(r_k) + \sum_{k=1}^{b_2} \psi_2(r_k) + \sum_{k=1}^{b_{12}} \phi(r_k) \tag{2}$$

where the first sum is over all two-atom bonds, b_1, of body $\hat{\Omega}_1$, the second sum is over all b_2 bonds of body $\hat{\Omega}_2$, and the last contribution is the sum over all b_{12} bonds involving one atom of each body. Further, ψ_1, ψ_2 and ϕ denote the interaction potentials of the three cases, which are considered to be different, since the two bodies may be comprised of atoms belonging to different elements. These two-point potentials only depend on the distance between atoms, i.e. the length of bond k, denoted by r_k. We term ψ the *intrasolid* potential, since it governs the interaction of atoms within the solid, and term ϕ the *intersolid* potential since it governs the interaction of atoms belonging to two distinct solids. Now, let us rewrite the internal energy (2) as

$$\hat{\Pi}_{\text{int}}(\mathscr{Z}) = \hat{\Pi}_{\text{int},1}(\mathscr{Z}_1) + \hat{\Pi}_{\text{int},2}(\mathscr{Z}_2) + \hat{\Pi}_{\text{int},12}(\mathscr{Z}) \tag{3}$$

where $\mathscr{Z}_1 = \{\mathbf{z}_i\}$, $i \in \mathscr{I}_1$ and $\mathscr{Z}_2 = \{\mathbf{z}_j\}$, $j \in \mathscr{I}_2$ are the collection of atomic positions in body 1 and 2. The sum over the bonds can be converted into a double sum over the atoms, so that the three contributions can be written as

$$\begin{aligned}
\hat{\Pi}_{\text{int},1} &:= \sum_{k}^{b_1} \psi_1(r_k) = \frac{1}{2} \sum_{i \in \mathscr{I}_1} \sum_{k \in \mathscr{I}_1}^{k \neq i} \psi_1(r_{ik}), \quad r_{ik} := |\mathbf{z}_i - \mathbf{z}_k| \\
\hat{\Pi}_{\text{int},2} &:= \sum_{k}^{b_2} \psi_2(r_k) = \frac{1}{2} \sum_{j \in \mathscr{I}_2} \sum_{\ell \in \mathscr{I}_2}^{\ell \neq j} \psi_2(r_{j\ell}), \quad r_{j\ell} := |\mathbf{z}_j - \mathbf{z}_\ell| \\
\hat{\Pi}_{\text{int},12} &:= \sum_{k}^{b_{12}} \phi(r_k) = \sum_{i \in \mathscr{I}_1} \sum_{j \in \mathscr{I}_2} \phi(r_{ij}), \quad r_{ij} := |\mathbf{z}_i - \mathbf{z}_j|
\end{aligned} \tag{4}$$

Note that a factor of $\frac{1}{2}$ is required in the first two equations, since each bond is counted twice in the double summation. This does not occur in the third equation, since the sets $\mathscr{I}_1$ and $\mathscr{I}_2$ are disjoint, hence no factor of $\frac{1}{2}$ is needed. In the equations above $\hat{\Pi}_{\text{int},1}$ and $\hat{\Pi}_{\text{int},2}$ denote the internal energy of bodies 1 and 2, and $\hat{\Pi}_{\text{int},12}$ denotes the interaction energy between the two bodies (which can be seen as an internal energy contribution of the entire system).

In the case of the external potential let as look at its variation which is written as

$$\delta\hat{\Pi}_{\text{ext}} = \sum_{i \in \mathscr{I}_1} \delta\mathbf{z}_i \cdot \mathbf{f}_i + \sum_{j \in \mathscr{I}_2} \delta\mathbf{z}_j \cdot \mathbf{f}_j \tag{5}$$

where $\mathbf{f}_i$ and $\mathbf{f}_j$ are the external forces acting on the atoms of body 1 and 2, and where $\delta\mathbf{z}_i$ and $\delta\mathbf{z}_j$ are the variations in the atomic positions. The kinetic energy of the discrete system is expressed as

$$\hat{K} = \frac{1}{2} \sum_{i \in \mathscr{I}_1} m_i |\dot{\mathbf{z}}_i|^2 + \frac{1}{2} \sum_{j \in \mathscr{I}_2} m_j |\dot{\mathbf{z}}_j|^2 \tag{6}$$

DOI: 10.1002/nme

given the atomic masses m_i, m_j and velocities $\dot{\mathbf{z}}_i$, $\dot{\mathbf{z}}_j$. With the energies defined above, the n_1+n_2 equilibrium equations of the discrete system follow from

$$\frac{\mathrm{d}}{\mathrm{d}t}\left(\frac{\partial \hat{L}}{\partial \dot{\mathbf{z}}_k}\right) - \frac{\partial \hat{L}}{\partial \mathbf{z}_k} = 0, \quad k = 1, \ldots, n_1 + n_2 \tag{7}$$

where $\hat{L} = \hat{K} - \hat{\Pi}$ is the Lagrangian of the system.

Now we would like to coarsen, or 'smear-out' the discrete system of atoms into a continuous medium, called a quasi-continuum since it is based on the underlying atomic system. The quasi-continuum is valid at an intermediate scale lying in between the atomic scale and the macroscale. The coarsening procedure, termed coarse-graining, is similar to the procedure of *smoothed particle hydrodynamics* used in meshfree methods, e.g. [28, 29].

Consider two continua with current configurations Ω_1 and Ω_2 corresponding to the discrete configurations $\hat{\Omega}_1$ and $\hat{\Omega}_2$. We define two co-ordinates $\mathbf{x}_1 \in \Omega_1$ and $\mathbf{x}_2 \in \Omega_2$, which are continuous functions within these domains. When no distinction between the two bodies is necessary, we can drop the subscripts and also write $\mathbf{z}_i \in \hat{\Omega}$ and $\mathbf{x} \in \Omega$. Given a function $g(\mathbf{x})$ defined on such a domain Ω, the discrete summation over the lattice sites $\mathbf{z}_i \in \mathscr{I}$ can be written as

$$\sum_{i \in \mathscr{I}} g(\mathbf{z}_i) = \int_\Omega \sum_{i \in \mathscr{I}} \delta(\mathbf{x} - \mathbf{z}_i)\ g(\mathbf{x})\, \mathrm{d}\Omega_{\mathbf{x}} \tag{8}$$

due to the property of the Dirac delta function $\delta(\mathbf{x} - \mathbf{z}_i)$. To coarsen the discrete field, we use the Gaussian distribution

$$\delta_h(\mathbf{y}) := \frac{1}{(\sqrt{\pi}h)^3} \exp\left(-\frac{\mathbf{y}\cdot\mathbf{y}}{h^2}\right) \tag{9}$$

also denoted as the coarse-graining function, to approximate the delta function δ in Equation (8) above. In can be verified that

$$\int_{\mathbb{R}^3} \delta_h(\mathbf{y})\, \mathrm{d}\Omega_{\mathbf{y}} = 1 \tag{10}$$

and $\delta_h(\mathbf{y}) \to \delta(\mathbf{y})$ as $h \to 0$. In passing, we note that other normalized, positive functions can be used as coarse-graining functions, e.g. see [30]. By using the distribution δ_h we can define the coarse-graining operation of a function $\hat{g}(\mathbf{x})$ as

$$g(\mathbf{x}) := \int_{\mathbb{R}^3} \delta_h(\mathbf{x} - \mathbf{y})\hat{g}(\mathbf{y})\, \mathrm{d}\Omega_{\mathbf{y}} \tag{11}$$

where the new function $g(\mathbf{x})$ can be seen as an approximation of $\hat{g}(\mathbf{x})$. The physical meaning of this operation is the weighted averaging over the support space $\mathscr{S}(\mathbf{x}) = \{\mathbf{y} | |\mathbf{x} - \mathbf{y}| \leqslant h\}$. From Equation (11) follows that the discrete particle density $\hat{\beta}(\mathbf{x})$ (measured in *number of particles per volume*) and mass density $\hat{\rho}(\mathbf{x})$, given by

$$\hat{\beta}(\mathbf{x}) := \sum_{i \in \mathscr{I}} \delta(\mathbf{x} - \mathbf{z}_i), \quad \hat{\rho}(\mathbf{x}) := \sum_{i \in \mathscr{I}} \delta(\mathbf{x} - \mathbf{z}_i) m_i \tag{12}$$

are coarse-grained into the smooth functions

$$\beta(\mathbf{x}) := \sum_{i \in \mathscr{I}} \delta_h(\mathbf{x} - \mathbf{z}_i), \quad \rho(\mathbf{x}) := \sum_{i \in \mathscr{I}} \delta_h(\mathbf{x} - \mathbf{z}_i) m_i \tag{13}$$

DOI: 10.1002/nme

Given these coarse-grained densities the discrete summation (8) can be approximated as

$$\sum_{i\in\mathscr{I}} g(\mathbf{z}_i) = \int_\Omega \hat{\beta}(\mathbf{x}) g(\mathbf{x})\, \mathrm{d}\Omega_{\mathbf{x}} \approx \int_\Omega \beta(\mathbf{x}) g(\mathbf{x})\, \mathrm{d}\Omega_{\mathbf{x}} \tag{14}$$

Clearly, as $h \to 0$ this approximation becomes exact. Equation (14) is also exact, for all h, if $g(\mathbf{x})$ is a constant or even linear function in $\mathbf{x}$, due to the symmetry of δ_h. Therefore, if h is chosen such that g is approximately linear within the support space $\mathscr{S}$, the accuracy of Equation (14) will be very good. In fact, according to this criteria, approximation (14) can be made arbitrarily accurate, thus enabling a seamless transition between MD and the CGCM.

Based on the coarse-graining of the discrete system, we now derive the Lagrangian of the quasi-continuum. In order to coarsen the internal energy $\hat{\Pi}_{\mathrm{int},I}$, $I = 1, 2$, given in Equation (4), let us introduce the function $\Psi(\mathbf{z}_i)$ such that the internal energy for both bodies can be written in the form

$$\hat{\Pi}_{\mathrm{int}} = \sum_{i\in\mathscr{I}} \Psi(\mathbf{z}_i), \quad \Psi(\mathbf{z}_i) := \frac{1}{2} \sum_{k\in\mathscr{I}}^{k\neq i} \psi(r_{ik}), \quad r_{ik} = |\mathbf{z}_i - \mathbf{z}_k| \tag{15}$$

With the definition of the particle density $\beta(\mathbf{x})$ in Equation (13) the internal energy is coarse-grained as

$$\begin{aligned} \hat{\Pi}_{\mathrm{int}} &= \int_\Omega \sum_{i\in\mathscr{I}} \delta(\mathbf{x} - \mathbf{z}_i)\Psi(\mathbf{x})\, \mathrm{d}\Omega_{\mathbf{x}} \approx \int_\Omega \sum_{i\in\mathscr{I}} \delta_h(\mathbf{x} - \mathbf{z}_i)\Psi(\mathbf{x})\, \mathrm{d}\Omega_{\mathbf{x}} \\ &= \int_\Omega \beta(\mathbf{x})\Psi(\mathbf{x})\, \mathrm{d}\Omega_{\mathbf{x}} =: \Pi_{\mathrm{int}} \end{aligned} \tag{16}$$

where

$$\Psi(\mathbf{x}) = \frac{1}{2} \sum_{k\in\mathscr{I}} \psi(r_k), \quad r_k = |\mathbf{x} - \mathbf{z}_k|, \quad \mathbf{z}_k \neq \mathbf{x} \tag{17}$$

is the continuous counterpart of the discrete function $\Psi(\mathbf{z}_i)$. We thus have obtained the continuum potential Π_{int} from the coarsening of the corresponding discrete potential $\hat{\Pi}_{\mathrm{int}}$. We note that for a deforming solid, the current interatomic distance r_k depends on the deformation gradient $\mathbf{F}$, so that we can write $\Psi = \Psi(\mathbf{F})$. In view of the usual expression of the internal energy Π_{int} for a hyperelastic continuum, the function $\Psi(\mathbf{F})$ can be associated with the strain energy density. The energy density per current volume and the energy density per reference volume follow as

$$w(\mathbf{F}) = \beta\Psi(\mathbf{F}), \quad W(\mathbf{F}) = \beta_0\Psi(\mathbf{F}) \tag{18}$$

where $\beta_0 = \beta/J$ denotes the atomic density of the reference configuration and where $J = \det\mathbf{F}$ is the Jacobian determinant of the deformation gradient.

Applying the coarsening procedure to the interaction energy $\hat{\Pi}_{\mathrm{int},12}$ we immediately obtain

$$\begin{aligned} \hat{\Pi}_{\mathrm{int},12} &= \sum_{i\in\mathscr{I}_1} \sum_{j\in\mathscr{I}_2} \phi(|\mathbf{z}_i - \mathbf{z}_j|) \\ &\approx \int_{\Omega_1}\int_{\Omega_2} \beta_1(\mathbf{x}_1)\beta_2(\mathbf{x}_2)\phi(|\mathbf{x}_1 - \mathbf{x}_2|)\, \mathrm{d}\Omega_{\mathbf{x}_1}\, \mathrm{d}\Omega_{\mathbf{x}_2} =: \Pi_{\mathrm{C}} \end{aligned} \tag{19}$$

DOI: 10.1002/nme

where Π_C denotes the interaction potential of the CGCM. We note that the interaction energy Π_C is implicitly dependent on $\mathbf{F}$, since the current integration domains Ω_1 and Ω_2 depend on the deformation.

Using the coarsening procedure once more, the variation of the discrete external energy $\delta\hat{\Pi}_{\text{ext}} = \delta\hat{\Pi}_{\text{ext},1} + \delta\hat{\Pi}_{\text{ext},2}$, given in Equation (5), can be approximated as

$$\delta\hat{\Pi}_{\text{ext},I} \approx \int_{\Omega_I} \delta\mathbf{x}_I \cdot \bar{\mathbf{b}}_I \, \mathrm{d}v + \int_{\Gamma_{t,I}} \delta\mathbf{x}_I \cdot \bar{\mathbf{t}}_I \, \mathrm{d}a =: \delta\Pi_{\text{ext},I} \tag{20}$$

where the external atomic forces $\mathbf{f}_I$ have been identified with applied body forces $\bar{\mathbf{b}}_I$ (per unit volume) acting on Ω_I and with applied tractions $\bar{\mathbf{t}}_I$ acting on $\Gamma_{t,I} \subset \partial\Omega_I$, the traction specified part of the boundary of Ω_I. The fields $\bar{\mathbf{t}}_I$ and $\bar{\mathbf{b}}_I$ are considered in a form such that $\delta\Pi_{\text{ext},I}$ is derivable from a potential $\Pi_{\text{ext},I}$. We remark that from the physical point of view, the traction boundary condition does not make much sense, since forces on the individual atoms can only be applied through the interaction with neighbouring atoms. The traction contribution to Π_{ext} can therefore be replaced by the interaction potential Π_C. However, it is useful to retain the traction boundary condition for numerical purposes and we will keep it for this reason.

Analogously to the coarse-graining of the potential energy the kinetic energy of the discrete system is approximated as

$$\begin{aligned}\hat{K} &= \sum_{i\in\mathscr{I}} m_i \, |\dot{\mathbf{z}}_i|^2 = \int_\Omega \sum_{i\in\mathscr{I}} \delta(\mathbf{x} - \mathbf{z}_i) m_i \, |\dot{\mathbf{x}}|^2 \, \mathrm{d}\Omega_{\mathbf{x}} \\ &\approx \int_\Omega \sum_{i\in\mathscr{I}} \delta_h(\mathbf{x} - \mathbf{z}_i) m_i \, |\dot{\mathbf{x}}|^2 \, \mathrm{d}\Omega_{\mathbf{x}} = \int_\Omega \rho(\mathbf{x}) \, |\dot{\mathbf{x}}|^2 \, \mathrm{d}\Omega_{\mathbf{x}} =: K\end{aligned} \tag{21}$$

where we omit the hat on K to indicate that it is the kinetic energy of the continuum.

With the coarsening given in Equations (16), (19), (20) and (21) we can write down the mesoscale Lagrangian of the quasi-continuum as

$$L = \sum_{I=1}^{2} [K_I - \Pi_{\text{int},I} + \Pi_{\text{ext},I}] - \Pi_C \tag{22}$$

with

$$\begin{aligned} K_I &= \frac{1}{2} \int_{\Omega_I} \rho_I(\mathbf{x}_I) |\dot{\mathbf{x}}_I|^2 \, \mathrm{d}v_I \\ \Pi_{\text{int},I} &= \int_{\Omega_I} w_I(\mathbf{F}_I) \, \mathrm{d}v_I \\ \Pi_C &= \int_{\Omega_1} \int_{\Omega_2} \beta_1(\mathbf{x}_1)\beta_2(\mathbf{x}_2)\phi(r) \, \mathrm{d}v_2 \, \mathrm{d}v_1, \quad r = |\mathbf{x}_1 - \mathbf{x}_2| \end{aligned} \tag{23}$$

and where $\Pi_{\text{ext},I}$ is the potential associated with the variation $\delta\Pi_{\text{ext},I}$. Note that the kinetic energy K_I and the internal and external energies $\Pi_{\text{int},I}$ and $\delta\Pi_{\text{ext},I}$ are in the same form as commonly considered in continuum mechanics. On the other hand, the potential Π_C is a new contribution modelling the interaction of the two separate continua. We note that the integration in Π_C is

DOI: 10.1002/nme

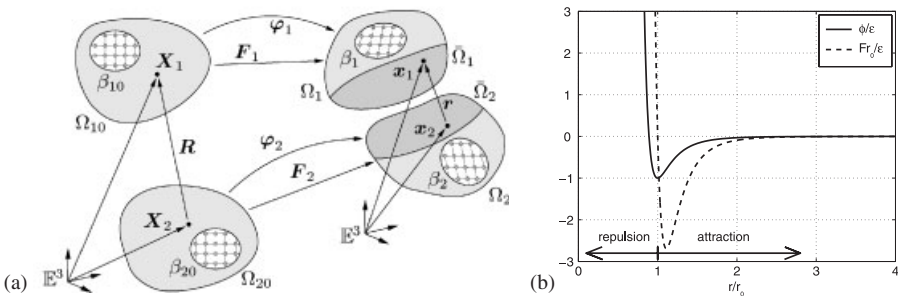

Figure 2. (a) Nanoscale contact description; and (b) Lennard-Jones potential.

over the current configuration of the deforming bodies, leading to a strong non-linear coupling of the behaviour of the two bodies. The study of the continuum interaction energy Π_C has a long history. The first work dates back to the 1930s by the prominent contributions of Bradley [31] and Hamaker [23], who evaluate integral $(23)_3$ for simple, rigid geometry such as two spherical particles Ω_1 and Ω_2. Recently, the interaction energy Π_C has also been considered in the study and simulation of CNTs. In the works of Arroyo and Belytschko [32, 33], the Cauchy–Born rule is extended to two-dimensional manifolds *via* the exponential map to model the response of deforming crystalline films. To model the non-bonded response of atoms, the authors consider an expression analogous to Equation $(23)_3$. In the work of Qian *et al.* [20] the interaction energy Π_C is used to model the interlayer response of multiwalled CNTs. Here, the authors motivate Π_C by its increased efficiency over the atomic summation of Equation (4). To the best of the authors' knowledge, a general finite deformation contact theory for small scales and its non-linear finite element implementation for arbitrarily shaped bodies, as is studied here, has not been given before. We also believe that, especially in three dimensions, the interaction energy Π_C has to be approximated further to increase the efficiency of large-scale computations. Such approximations are considered in Section 4, which discusses the implementation of the CGCM.

In summary, we remark that we have considered a simple spatial coarse-graining technique and that our approach can be generalized by including temporal coarse-graining and thermal effects, e.g. by using other coarse-graining functions δ_h [30, 34]. One may also consider an approach which distinguishes between the internal energy of surface atoms and the internal energy of bulk atoms. This is not studied here, however, the formalism of the present model can accommodate such an approach. We further stress that we have coarse-grained a discrete model into a continuum, whereas often the numerically motivated coarse-graining of a discrete system into a coarser discrete system is considered [34].

3.2. The variational weak formulation

Having obtained the coarse grained Lagrangian we can proceed deriving the corresponding weak form. Before we do so, we first show that the mesoscale Lagrangian, in particular contribution Π_C, can also be obtained directly from a continuum approach. Figure 2(a) shows the interaction of two bodies in the context of finite deformation continuum mechanics. Here, Ω_{10} and Ω_{20} are the reference configurations of the two bodies with the atomic densities β_{10} and β_{20}. These coarse grain densities have been introduced in the previous section. They depend on the atomic structure

DOI: 10.1002/nme

as is discussed in Section 3.3. For a given material, the reference densities β_{10} and β_{20} are given parameters. Further, in Figure 2, $\boldsymbol{\varphi}_1 = \mathbf{x}_1(\mathbf{X}_1, t)$ and $\boldsymbol{\varphi}_2 = \mathbf{x}_2(\mathbf{X}_2, t)$ are the motions mapping the reference configurations Ω_{10} and Ω_{20} onto the current configurations Ω_1 and Ω_2 of the two bodies. The atomic density in the current configuration is denoted by β_1 and β_2. The bodies are subjected to the usual prescribed displacement and traction boundary conditions. We consider two arbitrary points $\mathbf{x}_1 \in \Omega_1$ and $\mathbf{x}_2 \in \Omega_2$, whose distance is given by $r := |\mathbf{x}_1 - \mathbf{x}_2|$. In the proposed model, we assume that two atoms (or molecules) located at $\mathbf{x}_1$ and $\mathbf{x}_2$ interact with each other *via* an interatomic potential $\phi(r)$. In general, ϕ may be any potential suitable to describe the physical situation at hand, and one may find many different cases in the literature [21]. A popular choice is the Lennard-Jones potential

$$\phi(r) = \varepsilon \left(\frac{r_0}{r}\right)^{12} - 2\varepsilon \left(\frac{r_0}{r}\right)^{6} \tag{24}$$

where r_0 and ε are a length and an energy scale. The force $F(r)$ between the two atoms is then given by the gradient

$$F(r) = -\frac{\partial \phi}{\partial r} = \frac{12\varepsilon}{r_0} \left[\left(\frac{r_0}{r}\right)^{13} - \left(\frac{r_0}{r}\right)^{7} \right] \tag{25}$$

It can be seen that r_0 is the equilibrium distance between the atoms, i.e. the distance where $F = 0$, and that ε is the energy of the well at $r = r_0$. This well depth corresponds to the energy required to pull the two atoms apart from $r = r_0$ to ∞. A normalized graph of $\phi(r)$ and $F(r)$ is shown in Figure 2(b).

To set ϕ apart from the intrasolid potential ψ, let us also write $r_\phi := r_0$ and $\varepsilon_\phi := \varepsilon$. The parameters r_0 and ε are empirical material properties that have been listed in the literature for various materials. In case the two atoms belong to two distinct materials a and b with parameters r_0^a, r_0^b, ε_a and ε_b, the equilibrium distance and well depth of the combined system can be taken as the arithmetic and geometric mean

$$r_0^{ab} = \frac{r_0^a + r_0^b}{2}, \quad \varepsilon_{ab} = \sqrt{\varepsilon_a \varepsilon_b} \tag{26}$$

e.g. see [35]. Given $\phi(r)$, the total interaction between bodies Ω_1 and Ω_2 follows from the integration over all points $\mathbf{x}_1 \in \Omega_1$ and $\mathbf{x}_2 \in \Omega_2$. We thus obtain the interaction potential of the CGCM

$$\Pi_{\mathrm{C}} := \int_{\bar{\Omega}_1} \int_{\bar{\Omega}_2} \beta_1 \beta_2 \ \phi(r) \, \mathrm{d}v_2 \, \mathrm{d}v_1 \tag{27}$$

just as given in Equation $(23)_3$. Note that by choosing the integration domains $\bar{\Omega}_1 \subseteq \Omega_1$ and $\bar{\Omega}_2 \subseteq \Omega_2$, as shown in Figure 2(a), we have allowed for the possibility that the bodies only interact *via* these subsets. This is motivated by the fact that ϕ decays rapidly and may be neglected beyond a cutoff radius r_{c}. We note that the dependence of Π_{C} on the deformation of the two bodies Ω_1 and Ω_2 leads to a strong non-linear coupling between the bodies. Another salient property of Π_{C} is that it is strongly controlled by the gap between Ω_1 and Ω_2 since the interaction is strongest between closest points.

DOI: 10.1002/nme

For the quasi-continuum system shown in Figure 2, the total potential energy is given by

$$\Pi = \sum_{I=1}^{2} [\Pi_{\text{int},I} - \Pi_{\text{ext},I}] + \Pi_{\text{C}} \tag{28}$$

We note that in general, for a discrete lattice the system's potential energy $\hat{\Pi}$ (1)–(4), comprised of the summation of the individual atomic interaction potentials ψ and ϕ, is not convex and has many local minima, corresponding to several possible equilibrium configurations of the lattice. This non-convexity carries over to the potential Π of the interacting quasi-continua. The non-convex behaviour of the internal energy Π_{int} of the quasi-continuum has been noted by Tadmor *et al.* [16]. Depending on the shape of Ω_1 and Ω_2, the interaction potential Π_{C} will also contribute to the non-convex behaviour of Π. For instance, surface asperities lead to the non-convexity of Π_{C} [25]. For an appropriate refinement of the geometry of the bodies, it is possible to obtain local convexity.

Thus, for a quasi-static motion of the given conservative system, equilibrium follows from the principle of stationary potential energy, that is, from the stationary value of Π,

$$\delta\Pi = \sum_{I=1}^{2} [\delta\Pi_{\text{int},I} - \delta\Pi_{\text{ext},I}] + \delta\Pi_{\text{C}} = 0 \tag{29}$$

we obtain the weak form of the equilibrium equation. The variation of the internal energy $\Pi_{\text{int},I}$ of body I can be written as

$$\delta\Pi_{\text{int},I} = \int_{\Omega_I} \text{grad}(\delta\boldsymbol{\varphi}_I) : \boldsymbol{\sigma}_I \, \text{d}v_I \tag{30}$$

where grad(...) denotes the gradient with respect to the current configuration and where $\boldsymbol{\sigma}_I$ is the Cauchy stress tensor in body I. This stress follows from a particular choice of W as is considered in the following section. The variation of the external energy $\Pi_{\text{ext},I}$ is given by expression (20), where $\delta\mathbf{x}_I = \delta\boldsymbol{\varphi}_I$.

We now consider the variation of the interaction energy Π_{C}. The total number of atoms $n = \beta \, \text{d}v$ within the current volume element $\text{d}v = I\text{d}v$ is considered to be conserved during deformation, i.e.

$$\beta \, \text{d}v = \beta_0 \, \text{d}V = \text{const} \tag{31}$$

By virtue of the chain rule, the variation of Π_{C} then becomes

$$\delta\Pi_{\text{C}} = \int_{\bar{\Omega}_1} \int_{\bar{\Omega}_2} \beta_1 \beta_2 \left(\frac{\partial\phi(r)}{\partial\mathbf{x}_1} \cdot \delta\boldsymbol{\varphi}_1 + \frac{\partial\phi(r)}{\partial\mathbf{x}_2} \cdot \delta\boldsymbol{\varphi}_2 \right) \text{d}v_2 \, \text{d}v_1 \tag{32}$$

which can also be written as

$$\delta\Pi_{\text{C}} = -\int_{\bar{\Omega}_1} \delta\boldsymbol{\varphi}_1 \cdot \beta_1 \mathbf{b}_1 \, \text{d}v_1 - \int_{\bar{\Omega}_2} \delta\boldsymbol{\varphi}_2 \cdot \beta_2 \mathbf{b}_2 \, \text{d}v_2 \tag{33}$$

DOI: 10.1002/nme

where we have defined the body forces

$$\begin{aligned} \mathbf{b}_1(\mathbf{x}_1) &:= -\frac{\partial \Phi_2}{\partial \mathbf{x}_1}, \quad \Phi_2 := \int_{\bar{\Omega}_2} \beta_2 \phi(r)\, \mathrm{d}v_2 \\ \mathbf{b}_2(\mathbf{x}_2) &:= -\frac{\partial \Phi_1}{\partial \mathbf{x}_2}, \quad \Phi_1 := \int_{\bar{\Omega}_1} \beta_1\ \phi(r)\, \mathrm{d}v_1 \end{aligned} \tag{34}$$

The physical interpretation of Equations (33) and (34) is as follows: each body Ω_I $(I = 1, 2)$ is surrounded by a field Φ_I (see also Figure 1), which generates a body force within the other body. In other words the presence of body Ω_2 exerts a body force field, $\mathbf{b}_1$, on body Ω_1, whereas Ω_1 exerts the field $\mathbf{b}_2$ on Ω_2. We see that $\delta\Pi_{\mathrm{C}}$ has the same structure as the first part of $\delta\Pi_{\mathrm{ext},I}$, however, we emphasize that $\bar{\mathbf{b}}_I$ and $\mathbf{b}_I$ are conceptually different: the body forces $\mathbf{b}_I$ arise from the interaction of the two bodies of the considered system, $\bar{\mathbf{b}}_I$ on the other hand is considered imposed externally onto the system. An example for the latter case is the body forces arising from a immersing gravity field.

By applying the gradient operator to the integrand, Equation (34) can also be written as

$$\begin{aligned} \mathbf{b}_1(\mathbf{x}_1) &= +\int_{\bar{\Omega}_2} \beta_2 F(r)\bar{\mathbf{r}}\, \mathrm{d}v_2 \\ \mathbf{b}_2(\mathbf{x}_2) &= -\int_{\bar{\Omega}_1} \beta_1 F(r)\bar{\mathbf{r}}\, \mathrm{d}v_1 \end{aligned} \tag{35}$$

where $F = -\partial\phi/\partial r$ and the where unit vector $\bar{\mathbf{r}}$ is defined by

$$\mathbf{r} = \mathbf{x}_1 - \mathbf{x}_2, \quad r = |\mathbf{r}|, \quad \bar{\mathbf{r}} = \frac{\mathbf{r}}{r} \tag{36}$$

We remark that for any two points $\mathbf{x}_1$ and $\mathbf{x}_2$ the force $F(r)$ acting in between is equal in magnitude and opposite in direction. The body forces $\mathbf{b}_1$ and $\mathbf{b}_2$ acting at $\mathbf{x}_1$ and $\mathbf{x}_2$, however, are neither equal in magnitude nor act in opposing directions in general. The resultant forces on both bodies, obtained from integrating $\mathbf{b}_I$ over body Ω_I, are again equal in magnitude and act in opposite direction.

In general, the motion is time dependent, and the kinetic energy of both bodies, given in Equation $(23)_1$, must be included. The Lagrangian of the quasi-continuum model is given by Equation (22), and the weak form now follows from Hamilton's principle which states that the action

$$A = \int_{t_1}^{t_2} L\, \mathrm{d}t \tag{37}$$

attains its stationary value for the true solution among all kinematically admissible variations within the time interval $\{t_1, t_2\}$. Thus, from $\delta A = 0$ we obtain the weak formulation

$$\sum_{I=1}^{2} \left[\int_{\Omega_I} \delta\boldsymbol{\varphi}_I \cdot \rho_I \ddot{\mathbf{x}}_I\, \mathrm{d}v_I + \int_{\Omega_I} \mathrm{grad}(\delta\boldsymbol{\varphi}_I) : \boldsymbol{\sigma}_I\, \mathrm{d}v_I - \int_{\bar{\Omega}_I} \delta\boldsymbol{\varphi}_I \cdot \beta_I \mathbf{b}_I\, \mathrm{d}v_I - \delta\Pi_{\mathrm{ext},I} \right] = 0 \ \ \forall \delta\boldsymbol{\varphi}_I \tag{38}$$

of the contact problem illustrated in Figure 2.

DOI: 10.1002/nme

Before proceeding further, we consider two simple extensions to the theory presented above. Firstly, we may consider the interaction potential to be given by

$$\Pi_{\mathrm{C}} = \int_{\partial\bar{\Omega}_1} \int_{\partial\bar{\Omega}_2} \tilde{\beta}_1 \tilde{\beta}_2 \phi(r)\, \mathrm{d}a_2\, \mathrm{d}a_1 \tag{39}$$

Here, the two-body interaction is restricted to the surface subsets $\partial\bar{\Omega}_I \subseteq \partial\Omega_I$, a situation which arises for example from the interaction of two bodies with charged surfaces. In this formulation $\tilde{\beta}_I$ denotes the atomic surface density in *number of atoms per surface area*. For this case, the derivation of the weak form follows the same steps as above replacing $\bar{\Omega}_I$ by $\partial\bar{\Omega}_I$ and β_I by $\tilde{\beta}_I$. We thus obtain an analogous weak form statement as given in Equation (38), where $\mathbf{b}_I$ is now a surface traction acting on $\partial\bar{\Omega}_I$ and which arises from the neighbouring surface.

A further extension of the above result is to study the interaction among N bodies. If we consider any two of the N bodies to be interacting the same way as discussed above, the total multibody interaction potential will be

$$\Pi_{\mathrm{C}} = \frac{1}{2}\sum_{I}^{N}\sum_{J\neq I}^{N} \Pi_{\mathrm{C},IJ}, \quad \Pi_{\mathrm{C},IJ} = \int_{\bar{\Omega}_I}\int_{\bar{\Omega}_J} \beta_I \beta_J \phi(r)\, \mathrm{d}v_J\, \mathrm{d}v_I \tag{40}$$

Note that this multibody summation is analogous to the atomic summation in $\hat{\Pi}_{\mathrm{int},1}$ and $\hat{\Pi}_{\mathrm{int},2}$, given in Equation (4).

3.3. The Cauchy–Born rule

In this section, we shall briefly discuss a particular constitutive model supported by the Cauchy–Born rule, e.g. see [36, 37]. Under the assumption that the deformation is homogeneous within some neighbourhood, the deformation of a crystal lattice behaves as is shown in Figure 3(a). Then the vector $\mathbf{R}$ between two undeformed atomic sites is mapped onto the vector $\mathbf{r} = \mathbf{F}\mathbf{R}$ between two atoms in the deformed configuration.

Consider a given undeformed, representative crystal unit cell $\mathscr{S}_{\mathrm{c}}$ with atomic density β_0. Using the Cauchy–Born rule the stored energy function, given by Equation (18), can be restated as

$$W(\mathbf{F}) = \frac{\beta_0}{2}\sum_{k\in\mathscr{S}_{\mathrm{c}}} \psi(r_k), \quad r_k = |\mathbf{r}_k|, \quad \mathbf{r}_k = \mathbf{F}\mathbf{R}_k \tag{41}$$

where the summation runs over all atom pairs k within the unit cell $\mathscr{S}_{\mathrm{c}}$, which has to be sufficiently large to include the range of possible interactions. The simplest case is to consider interaction

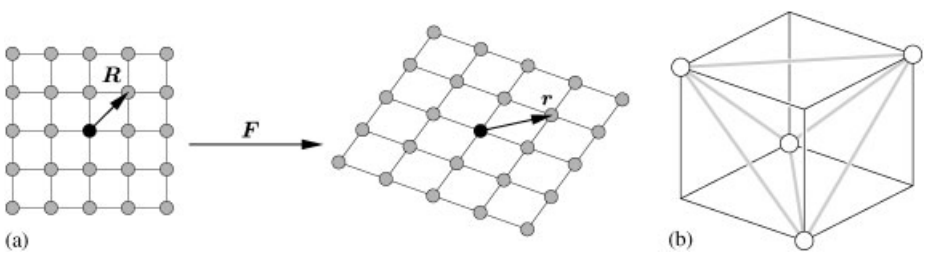

Figure 3. (a) Cauchy–Born rule; and (b) fcc nearest neighbour unit cell.

DOI: 10.1002/nme

between nearest neighbours only. For a face centred cubic (fcc) crystal the smallest possible unit cell $\mathscr{S}_c$ is displayed in Figure 3(b). The cell contains $k=6$ atomic bonds. The fcc crystal extends in space by reflection of this unit cell across its faces. As an example, the intrasolid interaction may be given by the Lennard-Jones potential

$$\psi(r)=\varepsilon_\psi\left(\frac{r_\psi}{r}\right)^{12}-2\varepsilon_\psi\left(\frac{r_\psi}{r}\right)^{6} \tag{42}$$

with well depth ε_ψ and equilibrium spacing r_ψ, which is the spacing of atoms in the undeformed configuration. For the considered unit cell the reference density is then given as

$$\beta_0=\frac{\sqrt{2}}{r_\psi^3} \tag{43}$$

From the stored energy function $W(\mathbf{F})$ the second Piola–Kirchhoff stress now follows as

$$\mathbf{S}=2\frac{\partial W}{\partial \mathbf{C}}=\beta_0\sum_{k\in\mathscr{S}_c}\frac{\partial\psi}{\partial r_k}\frac{\mathbf{R}_k\otimes\mathbf{R}_k}{r_k} \tag{44}$$

where $\mathbf{C}=\mathbf{F}^{\mathrm{T}}\mathbf{F}$ is the right Cauchy–Green tensor. Subsequently, the Cauchy stress can be expressed as

$$\boldsymbol{\sigma}=\frac{2}{J}\frac{\partial W}{\partial \mathbf{B}}\mathbf{B}=\beta\sum_{k\in\mathscr{S}_c}\frac{\partial\psi}{\partial r_k}\frac{\mathbf{r}_k\otimes\mathbf{r}_k}{r_k} \tag{45}$$

where $\mathbf{B}=\mathbf{F}\mathbf{F}^{\mathrm{T}}$ is the left Cauchy–Green tensor. The material and spatial tangent are then obtained as

$$\mathbb{C}=4\frac{\partial^2 W}{\partial \mathbf{C}^2}=\beta_0\sum_{k\in\mathscr{S}_c}\left(\frac{\partial^2\psi}{\partial {r_k}^2}-\frac{1}{r_k}\frac{\partial\psi}{\partial r_k}\right)\frac{\mathbf{R}_k\otimes\mathbf{R}_k\otimes\mathbf{R}_k\otimes\mathbf{R}_k}{r_k^2} \tag{46}$$

and

$$\mathbb{c}=\frac{4}{J}\mathbf{B}\frac{\partial^2 W}{\partial \mathbf{B}^2}\mathbf{B}=\beta\sum_{k\in\mathscr{S}_c}\left(\frac{\partial^2\psi}{\partial {r_k}^2}-\frac{1}{r_k}\frac{\partial\psi}{\partial r_k}\right)\frac{\mathbf{r}_k\otimes\mathbf{r}_k\otimes\mathbf{r}_k\otimes\mathbf{r}_k}{r_k^2} \tag{47}$$

We note that for a cubic crystal, as shown in Figure 3(b), the Cauchy–Born rule leads to a finite, anisotropic, cubic material law. We emphasize that this constitutive model is a local model and it only applies as long as the deformation is homogeneous within the considered unit cell. Highly inhomogeneous deformation, e.g. in the presence of dislocations, cannot be treated by the Cauchy–Born rule and we must then adopt a non-local formulation accounting for the varying deformation gradient $\mathbf{F}$ at the individual atomic sites. An approach combining the local and non-local formulations is the quasi-continuum method developed by Tadmor *et al.* [16]; see also [17, 22] for recent reviews. A mathematical study of the Cauchy–Born hypothesis can be found in [38].

We finally remark that the summation of potential ψ in Equation (41), can yield a non-convex function $W(\mathbf{F})$ with many local minima. However, it is reasonable to assume that a given crystal is initially stable, so that W will be convex in some neighbourhood around the undeformed configuration. This is the case for the shown fcc crystal.

DOI: 10.1002/nme

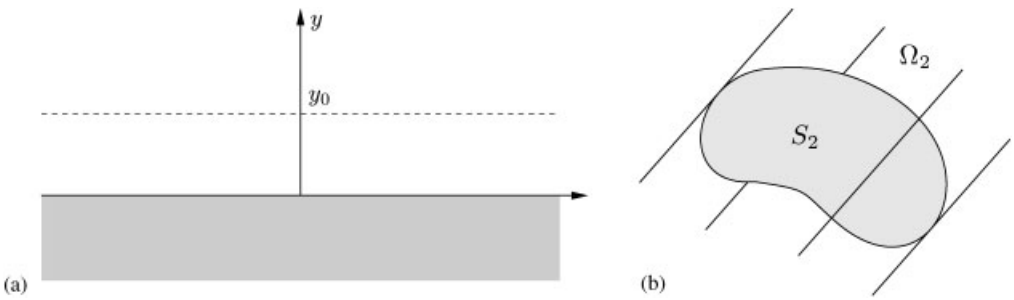

Figure 4. (a) Rigid half-space; and (b) plane strain cross section.

3.4. Analytical integration

In some cases the body forces (34), arising from the interaction between the two bodies, can be obtained by analytical integration. As an example let us consider the case where $\bar{\Omega}_2 = \Omega_2$ is given by the rigid, three-dimensional half-space displayed in Figure 4(a). By considering ϕ to be given by Equation (24) and supposing constant density β_2, the integration in Φ_2 $(34)_1$ can be carried out analytically, obtaining

$$\Phi_2 = \pi\beta_2\varepsilon r_0^3 \left[\frac{1}{45}\left(\frac{r_0}{y}\right)^9 - \frac{1}{3}\left(\frac{r_0}{y}\right)^3 \right] \tag{48}$$

The potential Φ_2 describes the interaction energy between the half-space and a point $\mathbf{x}_1$ at the distance y away from the half-space. The force acting at $\mathbf{x}_1$ follows as

$$F_{\Phi_2} = -\frac{\partial \Phi_2}{\partial y} = \pi\beta_2\varepsilon r_0^2 \left[\frac{1}{5}\left(\frac{r_0}{y}\right)^{10} - \left(\frac{r_0}{y}\right)^4 \right] \tag{49}$$

Compared to the potential $\phi(r)$ and the force $F(r)$ given in Equations (24) and (25), the exponents of the argument of the functions $\Phi_2(y)$ and $F_{\Phi_2}(y)$ decrease by three due to the volume integration. The equilibrium spacing between half-space and the point is $y_0 = r_0/\sqrt[6]{5}$.

We remark that, depending on the function $\phi(r)$, other simple shapes, like for example a rigid cylinder or sphere may also be integrated analytically.

A further important case is the case of plane strain, since it requires the use of analytical integration of ϕ. Figure 4(b) shows a three-dimensional body Ω_2 with an arbitrary cross section S_2, which is considered to be in the state of plane strain. The body force at $\mathbf{x}_1 \in \Omega_1$ can then be written as

$$\mathbf{b}_1(\mathbf{x}_1) = -\frac{\partial}{\partial \mathbf{x}_1} \int_{S_2} \beta_2 \hat{\phi}(r)\, \mathrm{d}a, \quad \hat{\phi}(r) := \int_{-\infty}^{\infty} \phi(r)\, \mathrm{d}z \tag{50}$$

where $\hat{\phi}(r)$ is the potential we obtain from integration along z, the direction perpendicular to S_2. An analogous expression follows for $\mathbf{b}_2$, the body force in body Ω_2. For the potential $\phi(r)$ given

DOI: 10.1002/nme

by Equation (24) we find

$$\hat{\phi}(r) = \pi\varepsilon r_0 \left[\frac{63}{256} \left(\frac{r_0}{r} \right)^{11} - \frac{3}{4} \left(\frac{r_0}{r} \right)^{5} \right] \tag{51}$$

and the corresponding force becomes

$$\hat{F}(r) = -\frac{\partial \hat{\phi}}{\partial r} = \pi\varepsilon \left[\frac{693}{256} \left(\frac{r_0}{r} \right)^{12} - \frac{15}{4} \left(\frac{r_0}{r} \right)^{6} \right] \tag{52}$$

We note that in Equations (51) and (52) above, the distance $r = |\mathbf{x}_1 - \mathbf{x}_2|$ refers to points $\mathbf{x}_1$ and $\mathbf{x}_2$ located within the plane strain cross section of the two bodies.

A similar analytical integration can be carried out for the case of axi-symmetry problems.

Furthermore, if both bodies are considered rigid, with constant density and simple geometry, the interaction potential Π_C can be fully integrated analytically, e.g. see [21, 23, 24, 31]. In some cases the interaction integration can also be simplified if infinitesimal deformations are assumed. A recent example is given in [39].

4. FINITE ELEMENT DISCRETIZATION

4.1. Method 1: the direct approach

The weak form (38) is implemented within the finite element method using an updated Lagrangian formulation, [19], due to its efficiency. The displacements $\mathbf{u} = \mathbf{x} - \mathbf{X}$ (and likewise the variation $\delta\boldsymbol{\varphi}$) are approximated by $\mathbf{u}(\mathbf{x}) \approx \sum_I N_I(\mathbf{x})\ \mathbf{u}_I$, a sum of the nodal displacements $\mathbf{u}_I$ and shape functions N_I. From Equation (38) the weak form of the discretized system can then be written as

$$\mathbf{v}^{\mathrm{T}}[\mathbf{M}\ddot{\mathbf{u}} + \mathbf{r}_{\mathrm{int}} + \mathbf{r}_{\mathrm{C}} - \mathbf{r}_{\mathrm{ext}}] = 0 \quad \forall \mathbf{v} \tag{53}$$

where $\mathbf{u}$ is the stacked vector of all nodal displacement $\mathbf{u}_I$, $\mathbf{v}$ is the stacked array of the variations $\delta\boldsymbol{\varphi}_I$, $\mathbf{M}$ is the mass matrix of the discretized system and $\mathbf{r} = \mathbf{r}_{\mathrm{int}} + \mathbf{r}_{\mathrm{C}} - \mathbf{r}_{\mathrm{ext}}$ is the nodal force vector. Since the equation above holds for all nodal variations $\delta\boldsymbol{\varphi}_I$ we obtain the discretized equations of motion

$$\mathbf{M}\ddot{\mathbf{u}} + \mathbf{r}(\mathbf{u}) = \mathbf{0}, \quad \mathbf{r}(\mathbf{u}) = \mathbf{r}_{\mathrm{int}}(\mathbf{u}) + \mathbf{r}_{\mathrm{C}}(\mathbf{u}) - \mathbf{r}_{\mathrm{ext}} \tag{54}$$

For a quasi-static problem we have $\ddot{\mathbf{u}} = \mathbf{0}$ and thus $\mathbf{r}(\mathbf{u}) = \mathbf{0}$. We therefore will also denote $\mathbf{r}$ as the residual. In the absence of external loading, as is considered in some of the later examples, we have $\mathbf{r}_{\mathrm{int}} + \mathbf{r}_{\mathrm{C}} = \mathbf{0}$, so that the problem becomes a balancing between internal and interaction forces (represented by the potentials ψ and ϕ).

In this section we focus on the contributions arising from the interaction potential Π_C given in Equation (27). To formulate the residual and stiffness corresponding to Π_C let us consider an element $\Omega_i^e \in \bar{\Omega}_1$ and an element $\Omega_j^e \in \bar{\Omega}_2$ as displayed in Figure 5(a). From $\delta\Pi_C$ (32) the residual contributions for element Ω_i^e and Ω_j^e can be derived as

$$\mathbf{r}_{C,i} = \int_{\Omega_i^e} \int_{\Omega_j^e} \mathbf{N}_i^{\mathrm{T}} \beta_i \beta_j \frac{\partial \phi}{\partial \mathbf{x}_i}\, \mathrm{d}v_j\, \mathrm{d}v_i, \quad \mathbf{r}_{C,j} = \int_{\Omega_i^e} \int_{\Omega_j^e} \mathbf{N}_j^{\mathrm{T}} \beta_i \beta_j \frac{\partial \phi}{\partial \mathbf{x}_j}\, \mathrm{d}v_j\, \mathrm{d}v_i \tag{55}$$

DOI: 10.1002/nme

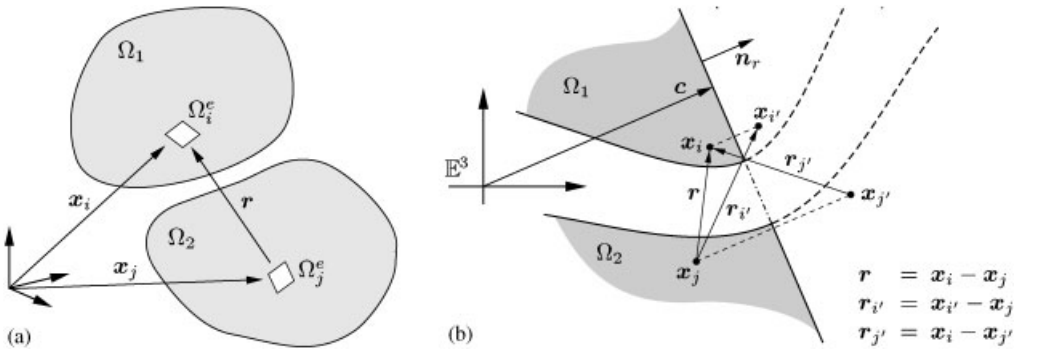

Figure 5. (a) Interacting elements; and (b) symmetry considerations.

(see [25]). These quantities correspond to the nodal force vectors acting on the two elements due to their mutual interaction. Here, $\mathbf{N}_i$ and $\mathbf{N}_j$ are arrays containing the shape functions of element Ω_i^e and Ω_j^e. Both $\mathbf{N}_i$ and $\mathbf{N}_j$ have the form

$$\mathbf{N} = [N_1\mathbf{I}, N_2\mathbf{I}, \ldots, N_n\mathbf{I}] \tag{56}$$

where n is the number of nodes per element and $\mathbf{I}$ is the identity tensor in $\mathbb{R}^3$. As has been noted in Equation (35), we have

$$\frac{\partial\phi}{\partial\mathbf{x}_i} = -F(r)\bar{\mathbf{r}}, \quad \frac{\partial\phi}{\partial\mathbf{x}_j} = F(r)\bar{\mathbf{r}} \tag{57}$$

with

$$\mathbf{r} = \mathbf{x}_i - \mathbf{x}_j, \quad r = |\mathbf{r}|, \quad \bar{\mathbf{r}} = \frac{\mathbf{r}}{r} \tag{58}$$

The total interaction force vector $\mathbf{r}_{\mathrm{C},i}^e$ of element Ω_i^e is the sum of the contributions $\mathbf{r}_{\mathrm{C},i}$ over all elements Ω_j^e. Likewise the total interaction force $\mathbf{r}_{\mathrm{C},j}^e$ of element Ω_j^e is the sum of the contributions $\mathbf{r}_{\mathrm{C},j}$ over all elements Ω_i^e. That is, we have

$$\mathbf{r}_{\mathrm{C},i}^e = \sum_{\Omega_j^e \in \bar{\Omega}_2} \mathbf{r}_{\mathrm{C},i}, \quad \mathbf{r}_{\mathrm{C},j}^e = \sum_{\Omega_i^e \in \bar{\Omega}_1} \mathbf{r}_{\mathrm{C},j} \tag{59}$$

To employ the Newton–Raphson method to solve the resulting non-linear equation, the tangent or stiffness matrix corresponding to Π_{C} is required. Linearizing $\mathbf{r}_{\mathrm{C},i}$ with respect to the degrees of freedom (dofs) of element Ω_i^e and Ω_j^e gives the two contributions

$$\begin{aligned} \mathbf{k}_{\mathrm{C},ii} &= \int_{\Omega_i^e}\int_{\Omega_j^e} \mathbf{N}_i^{\mathrm{T}}\beta_i\beta_j\frac{\partial^2\phi}{\partial\mathbf{x}_i\partial\mathbf{x}_i}\mathbf{N}_i \,\mathrm{d}v_j\,\mathrm{d}v_i \\ \mathbf{k}_{\mathrm{C},ij} &= \int_{\Omega_i^e}\int_{\Omega_j^e} \mathbf{N}_i^{\mathrm{T}}\beta_i\beta_j\frac{\partial^2\phi}{\partial\mathbf{x}_i\partial\mathbf{x}_j}\mathbf{N}_j \,\mathrm{d}v_j\,\mathrm{d}v_i \end{aligned} \tag{60}$$

DOI: 10.1002/nme

while the linearization of $\mathbf{r}_{\mathrm{C},j}$ w.r. to the dofs of element Ω_i^e and Ω_j^e yields

$$\begin{aligned}\mathbf{k}_{\mathrm{C},ji} &= \mathbf{k}_{\mathrm{C},ij}^{\mathrm{T}} \\ \mathbf{k}_{\mathrm{C},jj} &= \int_{\Omega_i^e}\int_{\Omega_j^e} \mathbf{N}_j^{\mathrm{T}} \beta_i \beta_j \frac{\partial^2 \phi}{\partial \mathbf{x}_j \partial \mathbf{x}_j} \mathbf{N}_j \, \mathrm{d}v_j \, \mathrm{d}v_i\end{aligned} \tag{61}$$

The mixed derivatives in the equations above can be written as

$$\begin{aligned}\frac{\partial^2 \phi(r)}{\partial \mathbf{x}_i \partial \mathbf{x}_j} &= \frac{F(r)}{r}\mathbf{I} + \left[F'(r) - \frac{F(r)}{r}\right] \bar{\mathbf{r}} \otimes \bar{\mathbf{r}} \\ \frac{\partial^2 \phi(r)}{\partial \mathbf{x}_i \partial \mathbf{x}_i} &= -\frac{\partial^2 \phi(r)}{\partial \mathbf{x}_i \partial \mathbf{x}_j} = \frac{\partial^2 \phi(r)}{\partial \mathbf{x}_j \partial \mathbf{x}_j}\end{aligned} \tag{62}$$

Finally, the total stiffness matrices $\mathbf{k}_{\mathrm{C},ii}^e$ and $\mathbf{k}_{\mathrm{C},jj}^e$ arising from the interaction between element Ω_i^e and body Ω_2, and between element Ω_j^e and body Ω_1, is obtained by the summation

$$\mathbf{k}_{\mathrm{C},ii}^e = \sum_{\Omega_j^e \in \bar{\Omega}_2} \mathbf{k}_{\mathrm{C},ii}, \quad \mathbf{k}_{\mathrm{C},jj}^e = \sum_{\Omega_i^e \in \bar{\Omega}_1} \mathbf{k}_{\mathrm{C},jj} \tag{63}$$

just as seen in Equation (59). No summation occurs for the off-diagonal contribution $\mathbf{k}_{\mathrm{C},ij}$, and we can write $\mathbf{k}_{\mathrm{C},ij}^e = \mathbf{k}_{\mathrm{C},ij}$. The global force vector $\mathbf{r}_{\mathrm{C}}$ and associated global stiffness matrix $\mathbf{K}_{\mathrm{C}}$ is obtained from the assembly of all contributions $\mathbf{r}_{\mathrm{C},i}^e$, $\mathbf{r}_{\mathrm{C},j}^e$, $\mathbf{k}_{\mathrm{C},ii}^e$, $\mathbf{k}_{\mathrm{C},ij}^e$, $\mathbf{k}_{\mathrm{C},ji}^e$ and $\mathbf{k}_{\mathrm{C},jj}^e$ of all elements $\Omega_i^e \in \bar{\Omega}_1$ and $\Omega_j^e \in \bar{\Omega}_2$.

We note that if $\bar{\Omega}_1 = \Omega_1$ and $\bar{\Omega}_2 = \Omega_2$, i.e. the interaction occurs between the entire domains, the global stiffness matrix will be completely filled in due to the interaction between all dofs of body Ω_1 and all dofs of body Ω_2. However, for cases where $\bar{\Omega}_1$ and $\bar{\Omega}_2$ are substantially smaller than their corresponding domains Ω_1 and Ω_2, the global stiffness matrix will be sparse. For cases where the physical situation demands that the entire domains interact with each other we propose two efficient approximations discussed in Section 4.2.

Due to the property $\mathbf{k}_{\mathrm{C},ji} = \mathbf{k}_{\mathrm{C},ij}^{\mathrm{T}}$ the global stiffness matrix is symmetric, as it should be since we are considering a conservative system.

Let us briefly remark on the case of a symmetric problem as is shown in Figure 5(b). Even though we may only model half of the system, we still have to account for the fact that the interaction reaches across the plane of symmetry. In other words the generic points $\mathbf{x}_i$ and $\mathbf{x}_j$ not only interact with each other, but also interact with the mirror images $\mathbf{x}_{j'}$ and $\mathbf{x}_{i'}$.

4.2. Approximate approaches: Method 2 and Method 3

In this section we propose two approaches to approximate the finite element formulation presented in Section 4.1. We shall refer to the original finite element formulation as Method 1 and denote the following two approximations by Method 2 and Method 3. We shall see that they are valid under certain, realistic assumptions and constitute more efficient and stable numerical methods. A quantitative comparison is shown in the following section. The basic idea of the two approximations is to introduce some form of analytical integration into the expressions for the force vector $\mathbf{r}_{\mathrm{C}}$ given in Equation (55). We do this without restricting the geometry in any way.

DOI: 10.1002/nme

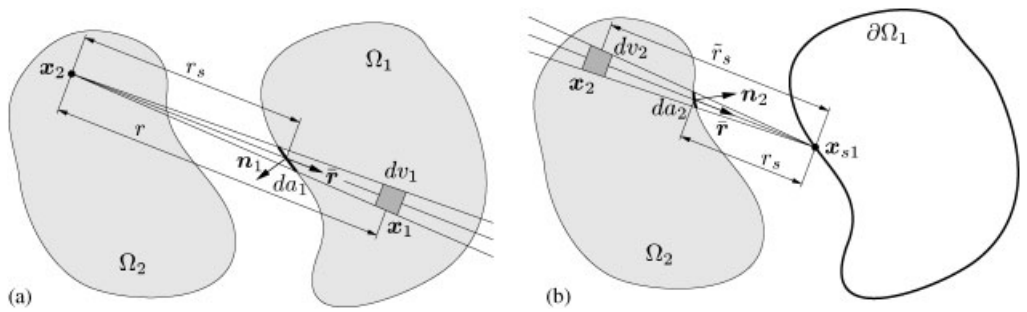

Figure 6. (a) Integration over Ω_1; and (b) integration over Ω_2.

The idea of Method 2 is to reduce the volume integration in $\mathbf{r}_C$ to a surface integration, by mapping the domain of interaction $\bar{\Omega}_I$ and the body forces $\mathbf{b}_I$ evoked inside the bodies onto the surface. To illustrate the method, we consider the case of plane strain where $\Omega_I \in \mathbb{R}^2$, for $I = 1, 2$, now refers to the cross section in plane strain. According to Figure 6 the volume elements of the two bodies can be written as

$$\mathrm{d}v_1 = \frac{r}{\tilde{r}_s}\,\mathrm{d}r\cos\alpha_1\,\mathrm{d}a_1, \quad \mathrm{d}v_2 = \frac{\tilde{r}_s}{r_s}\,\mathrm{d}\tilde{r}_s\cos\alpha_2\,\mathrm{d}a_2 \tag{64}$$

with $\cos\alpha_1 = -\bar{\mathbf{r}}\cdot\mathbf{n}_1$ and $\cos\alpha_2 = \bar{\mathbf{r}}\cdot\mathbf{n}_2$. The integration, say over Ω_1, can then be written as

$$\int_{\Omega_1}\ldots\mathrm{d}v_1 = \int_{\partial\Omega_1}\frac{1}{\tilde{r}_s}\int_{\tilde{r}_s}^{r_c} r\ldots\mathrm{d}r\cos\alpha_1\,\mathrm{d}a_1 \tag{65}$$

where r_c is the cutoff radius associated with $\phi(r)$. The integration scheme is valid for arbitrary r_c and we can set $r_c \to \infty$ for convenience. From Equation (64) we thus have

$$\mathrm{d}v_1\,\mathrm{d}v_2 = \frac{r}{r_s}\,\mathrm{d}r\,\mathrm{d}\bar{r}_s\cos\alpha_1\cos\alpha_2\,\mathrm{d}a_1\,\mathrm{d}a_2 \tag{66}$$

Here r_s is the distance between two surface points $\mathbf{x}_{s1}$ and $\mathbf{x}_{s2}$ written in the familiar structure

$$\mathbf{r}_s = \mathbf{x}_{s1} - \mathbf{x}_{s2}, \quad r_s = |\mathbf{r}_s|, \quad \bar{\mathbf{r}}_s = \frac{\mathbf{r}_s}{r_s} \tag{67}$$

Note that $\bar{\mathbf{r}}_s = \bar{\mathbf{r}}$. We now assume that the densities β_1 and β_2 are approximately constant along r. Substituting Equation (66) into (55), we obtain (see [25] for details)

$$\begin{aligned}\mathbf{r}_{C,i} &= -\int_{\Gamma_i^e}\int_{\Gamma_j^e}\mathbf{N}_i^{\mathrm{T}}\ \beta_i\beta_j\ F_s(r_s)\bar{\mathbf{r}}_s\cos\alpha_i\cos\alpha_j\,\mathrm{d}a_j\,\mathrm{d}a_i\\ \mathbf{r}_{C,j} &= +\int_{\Gamma_i^e}\int_{\Gamma_j^e}\mathbf{N}_j^{\mathrm{T}}\beta_i\beta_j F_s(r_s)\bar{\mathbf{r}}_s\cos\alpha_i\cos\alpha_j\,\mathrm{d}a_j\,\mathrm{d}a_i\end{aligned} \tag{68}$$

DOI: 10.1002/nme

for the contribution to the residual due to the interaction of two surface elements $\Gamma_i^e \in \partial\bar{\Omega}_1$ and $\Gamma_j^e \in \partial\bar{\Omega}_2$ with shape functions $\mathbf{N}_i$ and $\mathbf{N}_j$. Here, the force function

$$F_s(r_s) := \lim_{r_c\to\infty} \frac{1}{r_s} \int_{r_s}^{r_c} \int_{\tilde{r}_s}^{r_c} r\, F(r)\, \mathrm{d}r\, \mathrm{d}\tilde{r}_s \tag{69}$$

can be integrated analytically, if $F(r)$ is a simple function. In particular, for plane strain, where $F(r)$ is given by Equation (52), we find

$$\hat{F}_s(r_s) = \pi\varepsilon r_0^2 \left[\frac{77}{2560} \left(\frac{r_0}{r_s}\right)^{10} - \frac{5}{16} \left(\frac{r_0}{r_s}\right)^{4} \right] \tag{70}$$

where the hat indicates that we are considering a state of plane strain. Thus, with the steps above, we have reduced the volume integration of Equation (55) to the surface integration of Equation (68). It is noted that the arrays listed in (68) characterize the interaction between single surface elements. To obtain the interaction due to the entire surfaces an analogous summation scheme as listed in Equation (59) is required.

The cosine terms in Equation (68) can be replaced by $\cos\alpha_i = -\bar{\mathbf{r}}_s \cdot \mathbf{n}_i$ and $\cos\alpha_j = \bar{\mathbf{r}}_s \cdot \mathbf{n}_j$, where $\mathbf{n}_i$ and $\mathbf{n}_j$ are the outward normals of the current surface elements Γ_i^e and Γ_j^e. For practical integration purposes it is convenient to map the current integrals (68) back to the undeformed reference configuration Ω_{10} and Ω_{20}. Using Nanson's formula

$$\mathbf{n}\, \mathrm{d}a = J\mathbf{F}^{-T}\tilde{\mathbf{N}}\, \mathrm{d}A \tag{71}$$

where $\tilde{\mathbf{N}}\, \mathrm{d}A$ is the oriented surface element in the undeformed reference configuration. (The surface normal $\tilde{\mathbf{N}}$ should not be confused with the shape function array $\mathbf{N}$.) The spatial integrals (68) can then be expressed by the material integrals

$$\begin{aligned} \mathbf{r}_{C,i} &= -\int_{\Gamma_{i0}^e} \int_{\Gamma_{j0}^e} \mathbf{N}_i^{\mathrm{T}}\ \beta_{i0}\beta_{j0} F_s(r_s) \bar{\mathbf{r}}_s \theta_i \theta_j\, \mathrm{d}A_j\, \mathrm{d}A_i \\ \mathbf{r}_{C,j} &= +\int_{\Gamma_{i0}^e} \int_{\Gamma_{j0}^e} \mathbf{N}_j^{\mathrm{T}} \beta_{i0}\beta_{j0} F_s(r_s) \bar{\mathbf{r}}_s \theta_i \theta_j\, \mathrm{d}A_j\, \mathrm{d}A_i \end{aligned} \tag{72}$$

where Γ_{i0}^e, Γ_{j0}^e and β_{i0}, β_{j0} are referential quantities corresponding to their spatial counterparts. To simplify the notation we have introduced the two scalars

$$\theta_i := \bar{\mathbf{r}}_s \cdot \mathbf{F}_i^{-\mathrm{T}} \tilde{\mathbf{N}}_i, \quad \theta_j := \bar{\mathbf{r}}_s \cdot \mathbf{F}_j^{-\mathrm{T}} \tilde{\mathbf{N}}_j \tag{73}$$

where $\mathbf{F}_i$ and $\mathbf{F}_j$ are the deformation gradients within elements Γ_i^e and Γ_j^e. We remark that the linearization of integrals (72) is complicated by the parameters θ_i and θ_j. An approximate tangent to Equation (72) can be obtained by neglecting the contribution from $\theta_i\theta_j$. Such an approximation is believed to be very good, since the main variation of Equation (72) is caused by $F_s(r_s)$ rather than $\theta_i\theta_j$.

We remind that Method 2 is only valid if the assumption holds that the densities β_1 and β_2 are constant along r within the interaction zones $\bar{\Omega}_1$ and $\bar{\Omega}_2$. This is appropriate when the cutoff radius of $F(r)$ is very short compared to the distance over which the deformation of the body varies. Method 2 thus reduces the domain integration to a surface integration. We can say that

DOI: 10.1002/nme

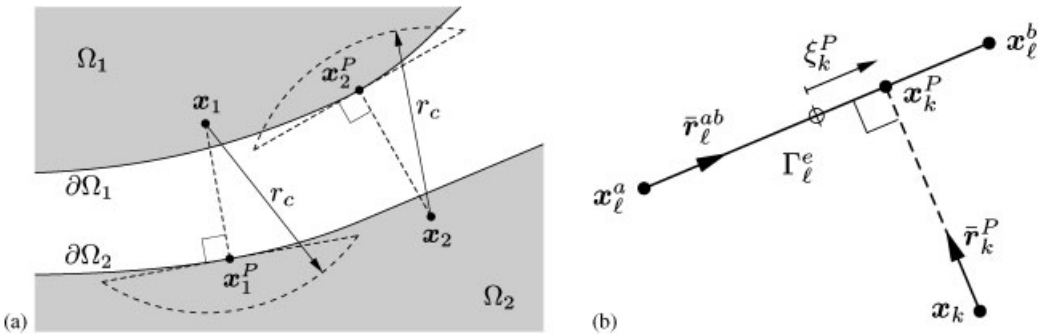

Figure 7. (a) Method 3; and (b) closest point projection.

the interaction of the two bodies is mapped onto their surfaces. In the context of infinitesimal deformations, a similar procedure has been derived in [40, 41].

Moreover, Method 2 can also be seen as an independent physical method to discretize Equation (39), i.e. the case for which the interactions are physically restricted to the surfaces. If the cosine terms are dropped and $\beta_i\beta_j F_\mathrm{s}$ is replaced by $\tilde{\beta}_i\tilde{\beta}_j F$, then Equation (68) corresponds to the discretization of the surface interaction formulation given by Equation (39).

Method 3 takes the analytical integration another step further. Consider the body force formulation of Equation (34). Let us rewrite this as

$$\mathbf{b}_k(\mathbf{x}_k) = -\frac{\partial \Phi_\ell}{\partial \mathbf{x}_k}, \quad \Phi_\ell = \int_{\bar{\Omega}_\ell} \beta_\ell \phi(r)\, \mathrm{d}v_\ell \tag{74}$$

for a point $\mathbf{x}_k \in \Omega_k$ influenced by the body Ω_ℓ. Here, we have either $\Omega_k = \Omega_1$, $\Omega_\ell = \Omega_2$ or $\Omega_k = \Omega_2$, $\Omega_\ell = \Omega_1$. Let us now suppose the two interacting bodies behave as illustrated in Figure 7(a), that is we consider that the curvature of the surfaces $\partial\Omega_1$ and $\partial\Omega_2$ is much smaller than the curvature of the cutoff radius r_c. We can then argue that, from the point of view of $\mathbf{x}_k$, the body Ω_ℓ can be approximated by a flat half-space located at the closest point projection, $\mathbf{x}_k^P$, of $\mathbf{x}_k$ onto $\partial\Omega_\ell$ and sharing the same tangent plane with Ω_ℓ at $\mathbf{x}_k^P$. We note that in a more refined version of Method 3, we can include the principal curvatures of surface $\partial\Omega_\ell$ for example by modelling Ω_ℓ at $\mathbf{x}_k^P$ as an ellipsoid. The projection of $\mathbf{x}_k$ onto $\mathbf{x}_k^P$ is shown in Figure 7(b) for the case where $\partial\Omega_\ell$ is discretized by linear, two-node elements Γ_ℓ^e (e.g. for the case of plane-strain or axi-symmetry). For this particular case, the projection of $\mathbf{x}_k$ is obtained as

$$\mathbf{x}_k^P = N_\ell^a(\xi_k^P)\mathbf{x}_\ell^a + N_\ell^b(\xi_k^P)\mathbf{x}_\ell^b \tag{75}$$

where N_ℓ^a and N_ℓ^b are the two linear shape functions of nodes $\mathbf{x}_\ell^a$ and $\mathbf{x}_\ell^b$ of element Γ_ℓ^e, and ξ_k^P is the location of $\mathbf{x}_k^P$ along this element. It is given by

$$\xi_k^P = \frac{(\mathbf{x}_\ell^b - \mathbf{x}_\ell^a)\cdot(2\mathbf{x}_k - \mathbf{x}_\ell^a - \mathbf{x}_\ell^b)}{(\mathbf{x}_\ell^b - \mathbf{x}_\ell^b)\cdot(\mathbf{x}_\ell^b - \mathbf{x}_\ell^a)} \tag{76}$$

DOI: 10.1002/nme

In the usual way, we define two normalized vectors along the projection and along the surface element, i.e.

$$\begin{aligned} \mathbf{r}_k^P &= \mathbf{x}_k^P - \mathbf{x}_k, \quad r_k^P = |\mathbf{r}_k^P|, \quad \bar{\mathbf{r}}_k^P = \frac{\mathbf{r}_k^P}{r_k^P} \\ \mathbf{r}_\ell^{ab} &= \mathbf{x}_\ell^b - \mathbf{x}_\ell^a, \quad r_\ell^{ab} = |\mathbf{r}_\ell^{ab}|, \quad \bar{\mathbf{r}}_\ell^{ab} = \frac{\mathbf{r}_\ell^{ab}}{r_\ell^{ab}} \end{aligned} \tag{77}$$

Approximating Ω_ℓ by some simpler shape with constant density we can rewrite Equation (74), as

$$\mathbf{b}_k(\mathbf{x}_k) = -\frac{\partial \Phi_\ell(r_k^P)}{\partial \mathbf{x}_k} = -\frac{\partial \Phi_\ell}{\partial r_k^P}\frac{\partial r_k^P}{\partial \mathbf{x}_k} = -F_\ell(r_k^P)\bar{\mathbf{r}}_k^P \tag{78}$$

where $\partial r_k^P/\partial \mathbf{x}_k = -\bar{\mathbf{r}}_k^P$ and $F_\ell := -\partial \Phi_\ell/\partial r_k^P$. We further assume that all these body forces within Ω_k, along the line defined by $\bar{\mathbf{r}}_k^P$, are projected onto the surface $\partial\Omega_k$. The force vector of surface element Γ_k^e can then be written as [25]

$$\mathbf{r}_{\mathrm{C},k}^e = \int_{\Gamma_k^e} \mathbf{N}_k^{\mathrm{T}} \beta_k F_{\mathrm{S}}(r_{\mathrm{S}}) \bar{\mathbf{r}}_k^P \cos\alpha_k \, \mathrm{d}a_k \tag{79}$$

where

$$F_{\mathrm{S}}(r_{\mathrm{S}}) := \lim_{r_{\mathrm{c}}\to\infty} \int_{r_{\mathrm{S}}}^{r_{\mathrm{c}}} F_\ell(r)\,\mathrm{d}r = \Phi_\ell(r_{\mathrm{S}}) \tag{80}$$

is the force function obtained by projecting F_ℓ onto the surface $\partial\Omega_k$. Here, r_{S} denotes the distance between $\mathbf{x}_k^P$ and $\partial\Omega_k$. If Ω_ℓ in the neighbourhood of $\mathbf{x}_k^P$ is approximated by a flat half-space (see Section 3.4), Φ_ℓ is given by (48) and the force F_{S} becomes

$$F_{\mathrm{S}} = \pi\beta_\ell \varepsilon r_0^3 \left[\frac{1}{45}\left(\frac{r_0}{r_{\mathrm{S}}}\right)^9 - \frac{1}{3}\left(\frac{r_0}{r_{\mathrm{S}}}\right)^3\right] \tag{81}$$

We remark that the above procedure applies to all surface elements on both surfaces $\partial\bar{\Omega}_1$ and $\partial\bar{\Omega}_2$. From the general arrangement of the two surfaces $\partial\bar{\Omega}_1$ and $\partial\bar{\Omega}_2$, it becomes apparent that the projection points $\mathbf{x}_1^P$, of $\mathbf{x}_1$ onto $\partial\bar{\Omega}_2$, and $\mathbf{x}_2^P$, of $\mathbf{x}_2$ onto $\partial\bar{\Omega}_1$, are independent of each other. Therefore, the global stiffness matrix $\mathbf{K}_{\mathrm{C}}$ obtained from the linearization of $\mathbf{r}_{\mathrm{C}}$, in general, will no longer be symmetric as is the case in Methods 1 and 2. However, it can be observed numerically, that the stiffness contribution $\mathbf{K}_{\mathrm{C}}$ (as well as the entire stiffness matrix $\mathbf{K}$) becomes symmetric at equilibrium, i.e. when the Newton–Raphson iteration as converged to zero residual $\mathbf{r} = \mathbf{0}$.

In summary, Section 4 presents three implementations of the CGC Model: Method 1—a volume interaction formulation, Method 2—a surface interaction formulation and Method 3—a point interaction formulation. Method 3 takes a similar approach as contact algorithms devised for macroscale problems, e.g. see [3], and it therefore provides a natural transition between the CGCM and the former. An investigation of the relation between the two and the application of Method 3 to macroscopic contact problems is addressed in [25].

DOI: 10.1002/nme

5. NUMERICAL EXAMPLES

This section serves as an illustration and validation of the proposed contact model and its three formulations mentioned above. For this we have constructed a simple, normalized benchmark problem. Further, in Section 5.4 we present results obtained by using actual material data.

5.1. A model problem

Consider the model problem of a cylinder, with radius R_0, located between two half-spaces, which are pushed together by a displacement u, as shown in Figure 8(a). We further consider the problem to be quasi-static and in a state of plane strain. Two discrete finite element models of the system, which exploit the symmetry of the problem, are shown in Figures 8(b) and (c). At the left, bottom and right boundary of the mesh we fix (imposed zero displacement) the dofs perpendicular to these surfaces, as indicated by the short black bars. The red bars at the top indicate dofs where the displacement u is prescribed. Apart from the deformation of the bodies we will monitor the load–displacement curve $P(u)$ and the evolution of the gap $g(u)$ between the tip of the indenter and the half-space below. To solve the problem we have used the three methods described earlier. Both the cylinder and half-space are modelled by the same hyperelastic material based on the Cauchy–Born rule. We consider a fcc crystal where only nearest neighbours are interacting *via* the intrasolid potential ψ given in Equation (42). The crystal unit cell of such a material is shown in Figure 3(b). We let this unit cell be aligned with the x, y and z (out of plane) axes of the model problem. The intersolid potential ϕ, governing the interaction between the two bodies, is modelled by Equation (24). Initially, this model problems depends on the parameters R_0, r_ψ, ε_ψ, r_ϕ and ε_ϕ. The quasi-static problem can be normalized by selecting a reference length and a reference energy. For this we chose the geometry parameter R_0 and the energy $E_0 := \beta_0 \varepsilon_\psi R_0^3$. The normalized problem can then be characterized by two parameters, the length and energy scale

$$\gamma_{\mathrm{L}} := \frac{R_0}{r_\phi}, \quad \gamma_{\mathrm{E}} := \frac{\varepsilon_\psi}{c_0 \varepsilon_\phi} \tag{82}$$

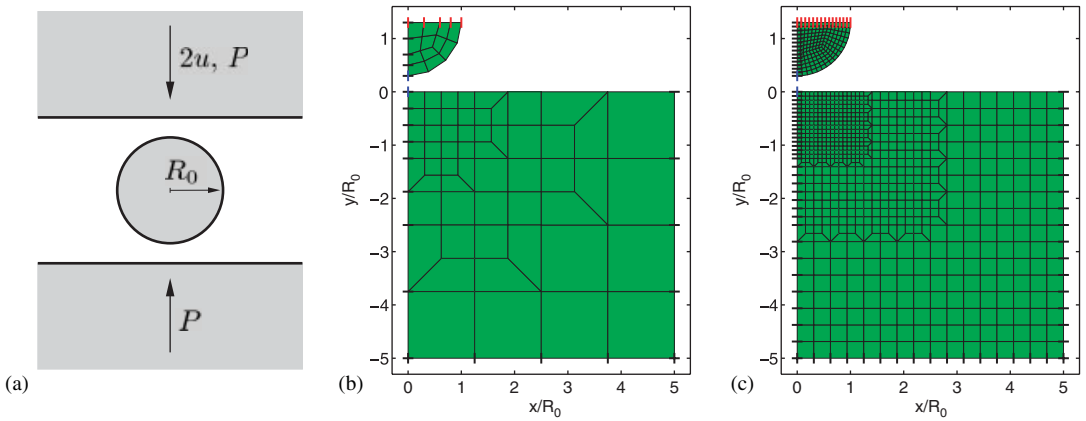

Figure 8. (a) Model problem; (b) coarse FE mesh; and (c) fine FE mesh.

DOI: 10.1002/nme

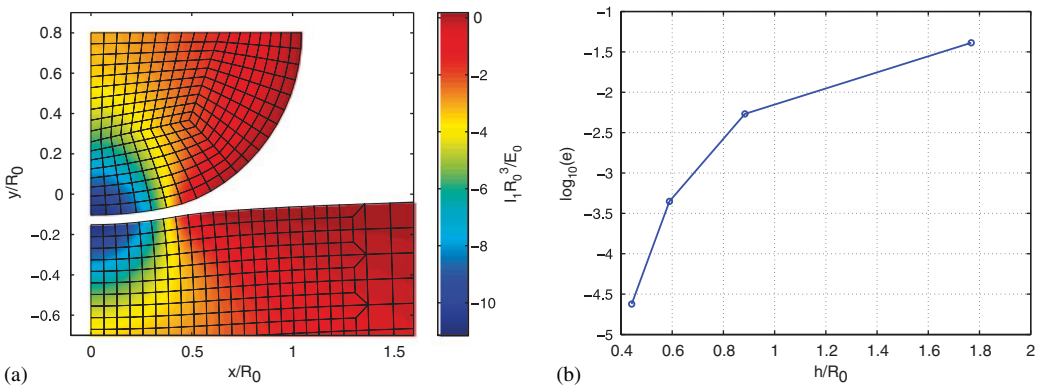

Figure 9. (a) Deformation and stress I_1; and (b) convergence of the FE solution.

where c_0 is a material constant defined as $c_0 := \beta_0 r_\phi^3$, which in view of Equation (43) becomes $c_0 = \sqrt{2} r_\phi^3 / r_\psi^3$. The length scale γ_L is the ratio between the cylinder radius R_0 and the equilibrium spacing r_ϕ of the potential ϕ, while the energy scale γ_E is proportional to the ratio of ε_ψ and ε_ϕ. We note that, upon normalization, the equilibrium distance r_ψ of potential ψ does not play any role in this model problem. The reason for this is that the crystal unit cell $\mathscr{S}_c$ can be normalized independently from the normalization of the problem geometry. Thus, we can normalize the unit cell by r_ψ even when the geometry is normalized by R_0. We note that this only works for the Cauchy–Born assumption that the deformation is homogeneous within the unit cell $\mathscr{S}_c$. It must only be assumed, that $\mathscr{S}_c$ is sufficiently small, such that the deformation can be considered homogeneous within the cell. We further consider a cutoff radius r_c beyond which the interaction force $F(r)$ (25) is negligible. At a given time/load step, the cutoff radius is selected such that F drops below $\frac{1}{1000}$ of the largest attractive force attained within the two bodies.

Figure 9(b) shows the rate of convergence of four successive meshes with largest element diameters $h_1 = 5\sqrt{2}R_0/4$, $h_2 = 5\sqrt{2}R_0/8$, $h_3 = 5\sqrt{2}R_0/12$ and $h_4 = 5\sqrt{2}R_0/16$ for an example using $\gamma_L = 10$ and $\gamma_E = 5$. Here, we have defined the error in the potential energy of the system as

$$e(h) := \frac{\Pi(h)}{\Pi(h_5)} - 1 \tag{83}$$

i.e. relative to a very fine mesh with $h_5 = 5\sqrt{2}R_0/20$. The deformed configuration and the stress invariant $I_1 = \operatorname{tr}\boldsymbol{\sigma}$ of the finest mesh are shown in Figure 9(a). Note that the stress I_1 has units E_0/R_0^3. The results are obtained from Method 1.

5.2. *Model problem results*

We now discuss some of the results of the model problem shown in Figure 8. The first result, obtained with Method 1 using the parameters $\gamma_L = 10/\sqrt[6]{2}$, and $\gamma_E = 5$, is shown in Figure 10. For these parameters a physical instability occurs during adhesion, as can be seen from the load–displacement curve $P(u)$ and the gap $g(u)$. In practice, there will be a jump between the stable branches of $P(u)$ and $g(u)$, a situation commonly denoted in the literature by jump-to-contact and jump-off-contact [12]. Furthermore, from Figure 10(a), one can see that for large u, P is not

DOI: 10.1002/nme

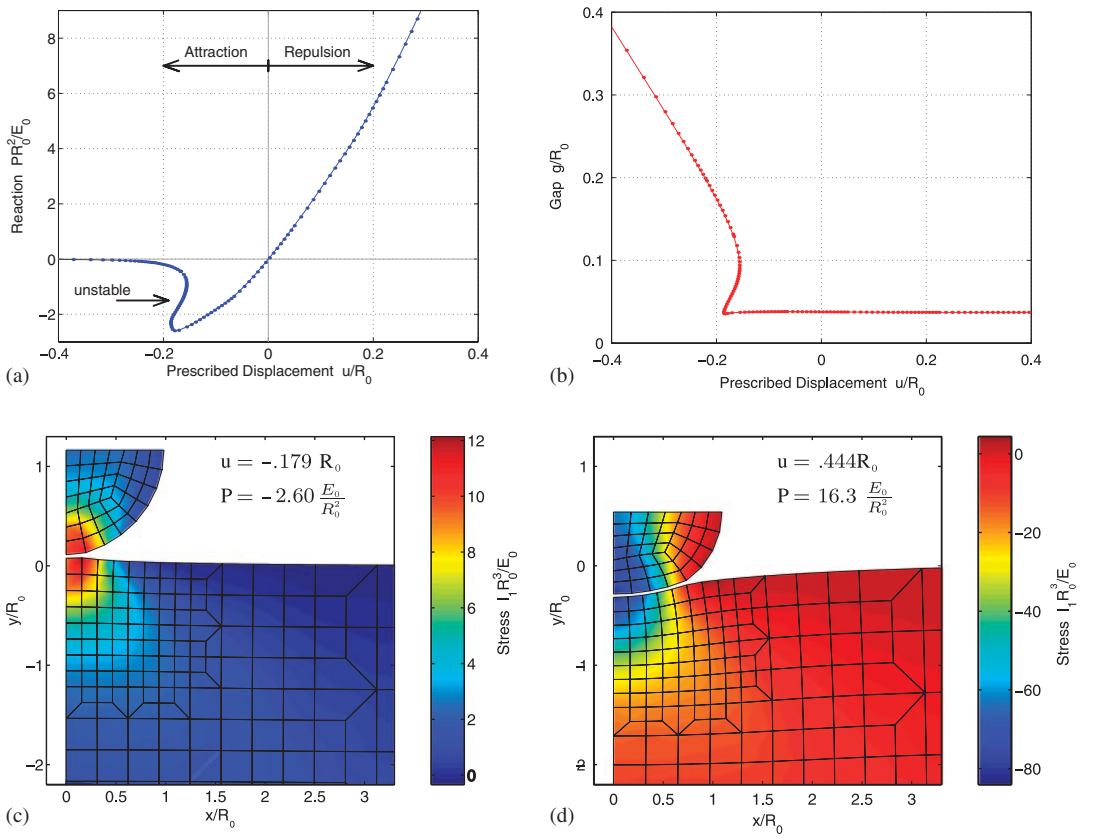

Figure 10. (a) Load–displacement curve; (b) gap between cylinder and half-space; (c) deformation and stress $I_1 = \mathrm{tr}(\boldsymbol{\sigma})$ during adhesion; and (d) deformation and stress I_1 during indentation.

linear but rather some power of u, which is in agreement to experimental indentation results [8] and analytical models [13, 14]. For large negative u, i.e. great separation distances, the force P between the bodies vanishes. The deformed bodies and the stress measure $I_1 = \mathrm{tr}(\boldsymbol{\sigma})$ is shown in Figures 10(c) and (d) for the specified values of u and P. Here, (c) shows the attraction as the bodies adhere, leading to strong tensile stress, whereas (d) shows the repulsion during indentation, giving large compressive stress. We remark that the adhesive stability is controlled by the ratio between the stiffness associated with the interaction energy Π_C and the stiffness associated with the elastic energy Π_{int}. In [25] it is shown that this stiffness ratio is controlled by the parameter $\gamma_K = \gamma_E/\gamma_L$: For small γ_K the bodies are relatively soft, and the system develops an instability; for large γ_K the bodies are too stiff for the system to become unstable. The size of the gap between the two bodies is controlled by γ_L. The gap decreases for increasing γ_L, i.e. if the atomic equilibrium spacing r_ϕ becomes smaller compared to the problem size given by R_0. We note that the gap is only slightly affected by γ_E.

As a second example we consider the parameters $\gamma_L = 25$, $\gamma_E = 5$, for which no instability occurs, and show a comparison between Methods 1–3. The load–displacement curve $P(u)$ and the gap

DOI: 10.1002/nme

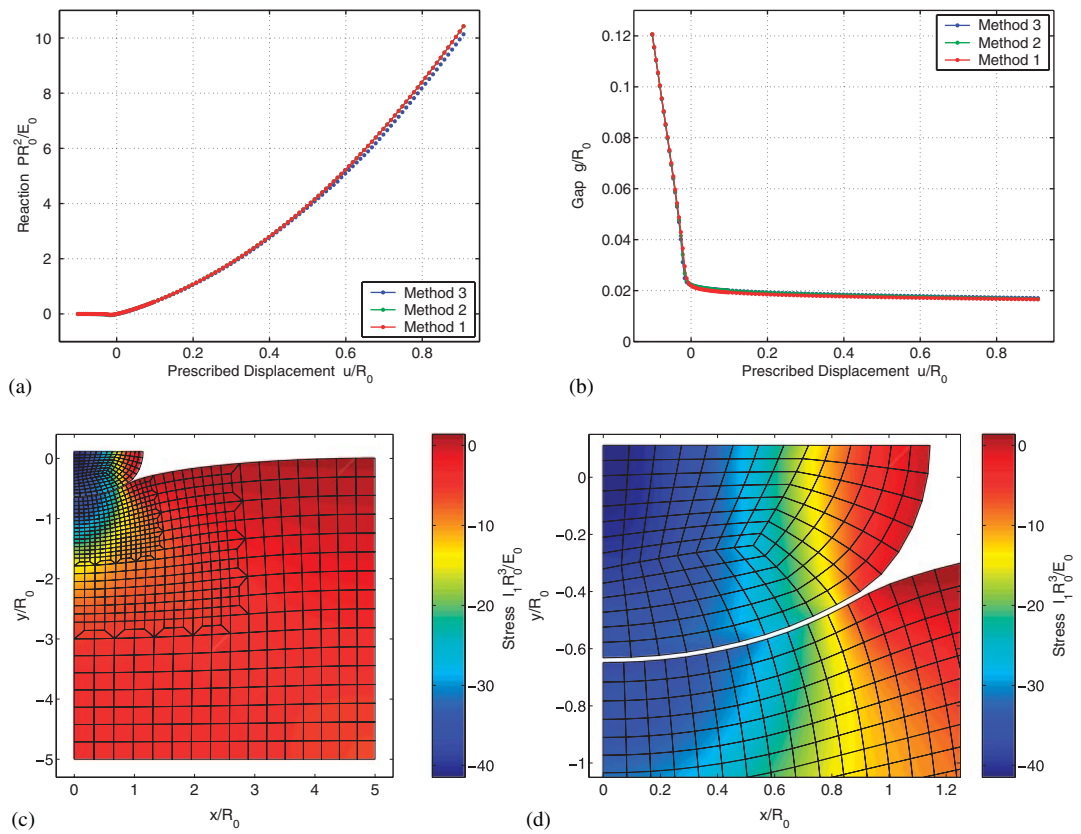

Figure 11. (a) Load–displacement curve; (b) gap between cylinder and half-space; (c) deformation and stress $I_1 = \mathrm{tr}(\boldsymbol{\sigma})$ for $u = 0.91R_0$; and (d) enlargement of c.

$g(u)$ for the three methods are shown in Figures 11(a) and (b). It can be seen that the force pushing down on the cylinder, $P(u)$, and the gap between cylinder and half-space, $g(u)$, are practically equal for all three methods. A small difference can be seen for $P(u)$ between Method 3 and the other two methods, Method 1 and 2, which are indistinguishable in Figure 11(a). The step size chosen in this simulation is $\Delta u = 0.005R_0$ and it is increased to $\Delta u = 0.01R_0$ after 40 steps for all methods. We have further used 5×5 quadrature points for the volume integration of Method 1, 5 quadrature points per surface element of Method 2 and only 2 quadrature points for the surface integration of Method 3. We note that we cannot use fewer quadrature points in Methods 1 and 2, since this will make the simulation numerically unstable. Effectively, the quadrature points will be too far apart to 'feel' each other. Method 3 does not have this drawback. It runs stable for only two quadrature points per surface element. The deformed mesh and the stress I_1 is shown in Figures 11(c) and (d) using Method 3 for $u = 0.91R_0$. The enlargement (d) shows how small the gap is for the chosen parameters. Considering that r_ϕ may be of the order of 0.5 nm, R_0 becomes of the order of 10 nm in this example.

In the following we illustrate the interaction between the two bodies from the numerical point of view. Considering Method 1, Figure 12(a) shows the deformed FE mesh for the parameters

DOI: 10.1002/nme

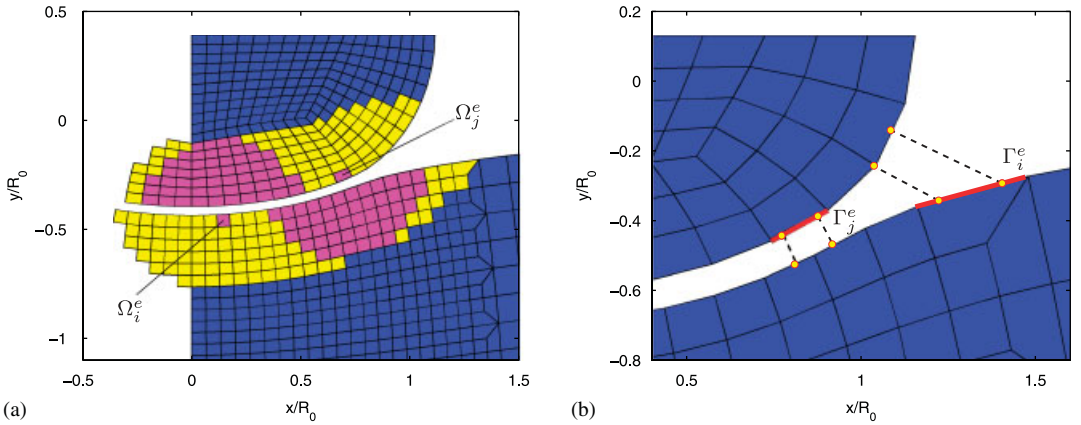

Figure 12. (a) Interaction zones for Method 1; and (b) projected Gauss points for Method 3.

Table I. Computational efficiency of the coarse-grained contact model.

	MD	M1	M2	M3
Number of dofs	258 000	1872	1872	1872
Number of intrasolid interactions	1.55×10^6	20 736	20 736	20 736
Number of intersolid interactions	5.0×10^6	231 875	2025	96

$\gamma_L = 10$ and $\gamma_E = 5$. The region formed by the yellow and pink element is a discrete snapshot of the current interaction domains $\bar{\Omega}_1$ and $\bar{\Omega}_2$. As has been argued in Section 4, these domains reach across the symmetry boundary. The interaction domains for two elements is shown. Element Ω_i^e interacts with the hemispherical region above, while Ω_j^e interacts with the zone below. A search algorithm is implemented which computes the interacting region for each element $\Omega_i^e \in \bar{\Omega}_I$, $I = 1, 2$. During subsequent loading these regions are updated. Figure 12(a) can also be used to illustrate the interaction implemented in Method 2. In this method the interacting domains $\partial\bar{\Omega}_1$ and $\partial\bar{\Omega}_2$ are formed by the exterior surface of $\bar{\Omega}_1$ and $\bar{\Omega}_2$. The interaction as derived in Method 3 is shown in Figure 12(b) for the values $\gamma_L = 5$ and $\gamma_E = 5$. The quadrature points of surface elements Ω_i^e and Ω_j^e are projected onto the closest point on the neighbouring surface as shown. Note that this projection is not always perpendicular to the surface we are projecting onto. As is seen for the first quadrature point of Ω_i^e, the closest projection point is a FE node.

Finally, Table I assesses the efficiency of the three methods of the CGCM, designated as 'M1' through 'M3' compared to a full molecular approach ('MD'). We consider the example shown in Figure 11 ($\gamma_L = 25$, $\gamma_E = 5$). The finite element discretization contains 1872 dofs and 864 elements. For the sake of comparison let us assume that the equilibrium spacing of the fcc lattice is $r_\psi = r_\phi/2$, i.e. half of the equilibrium spacing of the intersolid interaction ϕ. It follows that in the undeformed configuration there are $50\sqrt{2}$ atoms contained along the length R_0. The quarter system of Figure 11(c) thus contains around 129 000 atoms corresponding to 258 000 dofs for a state of plane strain. Considering only nearest neighbour intrasolid interaction, each atom interacts with a shell

DOI: 10.1002/nme

of 12 surrounding atoms, giving a total of about 1.55 million intrasolid interaction as stated in Table I. The Cauchy–Born rule, on the other hand, lets us reduce the number of interactions to six per unit cell (see Figure 3(b)). The total number of intrasolid interaction for the quasi-continuum then follows as 20 736 (considering a 2×2 quadrature rule to compute $\mathbf{r}_{\text{int}}$ for each element). The difference of the three methods comes into play when looking at the number of intersolid interactions. For Methods 1 and 2 we can count 371 and 81, respectively, element pairs of body 1 and 2 interacting with each other. For the considered quadrature rules to compute $\mathbf{r}_{\text{C}}$ (5×5 points for each volume element Ω_i^e of M1 and 5 points for each surface element Γ_i^e of M2) then follow the numbers given in Table I. For Method 3 the interaction needs only to be computed for the 96 quadrature points spread over the 48 surface elements constituting $\partial\Omega_1$ and $\partial\Omega_2$. This stands in strong contrast to the estimated 5 million intersolid interactions required for the molecular solution.

According to Table I it can be summarized that the number of dofs reduces by a factor of 138 from a full molecular model to the CGC Model. Likewise, the number of intrasolid interactions is reduced by a factor of 75. Between the molecular model and Method 1, the reduction in the number of intersolid interactions is about 22, from Method 1 to Method 2 it is a further 115 and from Method 2 to Method 3 the reduction factor is about 21. We note that the computational cost to set up $\mathbf{r}_{\text{int}}$ and $\mathbf{r}_{\text{C}}$ scales linearly with the number of intrasolid and intersolid interaction. Table I thus shows the huge gains in efficiency between the full atomistic approach and Methods 1–3. The number of dofs affects the solution time to solve the resulting equations of motion.

We emphasize that the comparison of Table I is by no means exhaustive, as it is restricted to quasi-static, temperature independent conditions. The efficiency also depends on the chosen scale, represented by γ_{L}. For small γ_{L} the savings compared to the molecular model will be much lower, indicating that the more accurate, molecular model becomes the method of choice. On the other hand as γ_{L} increases the efficiency of the presented CGCM, in particular Method 3, will become even more dramatic.

5.3. Discussion

Let us now summarize some of the key findings from the study of the simple model problem depicted in Figure 8.

1. Physically, the problem is only controlled by two parameters: γ_{L}, representing the geometry, and γ_{E}, representing the relative strength between ϕ and ψ. (Recall that we have fixed some other parameters by considering both bodies to be of the same anisotropic material, governed by the Cauchy–Born rule, with material axis aligned along x, y and z. Additional numerical parameters are the finite element mesh, the density of quadrature points and the cutoff radius r_{c} of the potential.)
2. If the two interacting bodies are soft compared to the strength of their mutual interaction an instability occurs during adhesion. This behaviour is controlled by the stiffness parameter $\gamma_K := \gamma_{\text{E}}/\gamma_{\text{L}}$.
3. The parameter γ_{L} controls the length scale of the contact problem, and for the proposed model to be applicable, γ_{L} has to be within a certain range. If γ_{L} becomes too small, the finite element resolution approaches the atomic resolution, and it will thus make more sense to use MD. On the other hand as γ_{L} becomes large we need smaller and smaller finite elements (or more and more quadrature points per element) to numerically refine the atomic interaction potential ϕ. In this case it will be more efficient to model contact by traditional means, i.e.

DOI: 10.1002/nme

not based on atomic interaction but rather based on a macroscopic impenetrability constraint. In other words the CGCM lives between two limit cases as has been argued in Section 2.

4. We note that for our model to be algorithmically stable, there is a limit on the load step size Δu (or time step size Δt for dynamic problems). In principle Δu should not be larger that the gap g, since this would result in the intersection of both bodies, letting the method fail. The load or time step can be increased significantly if an algorithmic treatment is included, that pushes the bodies apart in the case of intersection, e.g. by a penalty-type approach [25].
5. Methods 1 and 2 are sensitive to the number of Gauss points used to integrate Π_C. Using too few quadrature points can lead to the failure of the method since the quadrature points are too far apart to feel each other, an issue which has also been noted in [33]. In this respect, Method 3 is much more robust. Less refinement is required for the stable numerical integration of Method 3.
6. The three methods can be ordered based on their different nature. For small γ_L Method 1 will be most appropriate since in this case the interaction zones $\bar{\Omega}_1$ and $\bar{\Omega}_2$ are large and the deformation may vary strongly within these zones. A situation which cannot be captured by Method 2 or 3. On the other hand, for large γ_L the interaction zones are confined to the surface so that Methods 2 and 3 will constitute much more efficient schemes than Method 1 (e.g. see Table I). Thus, as γ_L increases we should also increase the numerical treatment from Method 1 to Method 3. Below Method 1, a MD approach will be more suitable, whereas beyond Method 3 conventional computational contact mechanics models should be used. (We note that Method 3 can in fact be seen as one of those [25].)

5.4. Application to carbon nanotubes

As an application of the CGC Model, we consider the deformation of a (40, 40) CNT cross section under plane strain conditions; for a CNT review see [42]. The tube consists of a hexagonal graphene structure with 160 carbon atoms around the circumference. The intersolid potential parameters are chosen as $r_\phi = 0.383$ nm and $\varepsilon_\phi = 2.39$ meV. The tube is modelled linear elastically with Young's modulus $E = 5.0$ T Pa, Poisson ratio $\nu = 0.19$ and wall thickness $t = 0.075$ nm. See [43] for a proposed range of material parameters.

Figure 13 shows the undeformed tube (a), its interaction with a rigid graphite substrate (b), with neighbouring tubes in a bundle (d) and with itself as it collapses (c). All equilibrium configurations

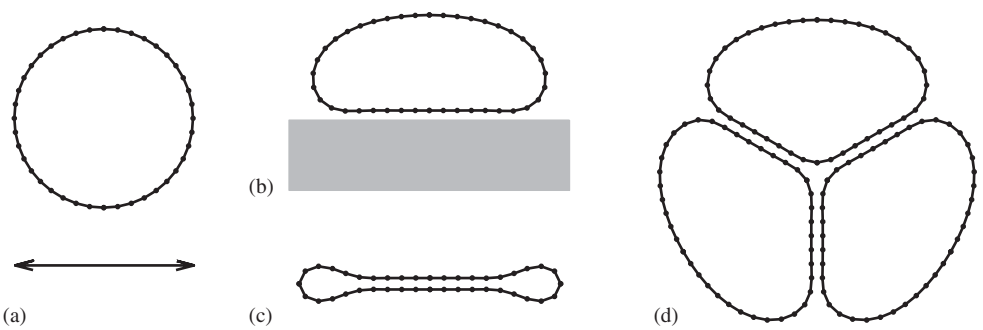

Figure 13. (a) Undeformed (40, 40) CNT; (b) adhesion of the CNT to a rigid substrate; (c) self collapse of the CNT; and (d) adhesion of three CNT's.

DOI: 10.1002/nme

shown are stable and drawn to scale. The tube is modelled by 40 geometrically exact 2-node beam elements, derived in the works of [44–46]. The dots shown in the figures indicate the FE nodes. Dynamic relaxation is used to obtain the deformed configurations. The results shown in Figure 13 are in agreement with the literature. A MD solution of case (b), the adhesion of the CNT to a rigid substrate can be found in [6, 47]. Molecular simulations of the collapsing CNT have been obtained by Gao *et al.* [5] and Tang *et al.* [48], a finite element solution can be found in [43, 49]. Experimental data showing the interaction of two CNT can be found in [50].

We note that, using simplifying assumptions on the geometry, the CNT self-collapse can also be studied by analytical means, e.g. see [48, 51]. It may be noted that Figures 13(a) and (c) show that the ring itself has two stable equilibrium positions, i.e. the potential energy Π has at least two local minima. In principle, if we consider a very stiff ring, there will be only one stable configuration, namely the undeformed ring. As the stiffness of the ring becomes softer more local minima of Π will appear. For very small ring stiffness, one can imagine that there are many 'collapsed' configurations.

We finally note that the complex, three-dimensional behaviour of interacting CNT, as is for example observed in [52], has been studied in much greater detail by the works of Arroyo and Belytschko [32, 33] and Qian *et al.* [20, 53].

6. CONCLUSION

In this paper, we have presented a quasi-continuum contact approach, termed the Coarse-Grained Contact Model (CGCM). The model is motivated both from the underlying molecular description and from the macroscale continuum mechanics approach. The model describes the interaction of solids based on the interaction of individual atoms belonging to the bodies. In our model, the atomic interaction potential is divided into two cases, the *intrasolid* potential, furnishing a constitutive relation for the continua, and the *intersolid* potential, determining the interaction between distinct bodies (or remote regions of the same body). The CGCM is implemented in an updated Lagrangian finite element formulation, and we have presented three variations of the implementation, termed Method 1–Method 3. We showed that, as the length scale of the problem increases, the approximations introduced in Methods 2 and 3 become increasingly appropriate: For large-scale problems we should use Method 3, since it is the most efficient, whereas at small scales we need to use Method 1, since it is more accurate. Computationally, the interaction between two bodies leads to the coupling of the dofs of the two bodies. Even if the interaction is confined to the neighbouring regions $\bar{\Omega}_1$ and $\bar{\Omega}_2$, the coupling can still affect a large number of dofs, as is shown in Table I.

We have illustrated the behaviour of the CGCM and its implementations through a simple model problem, which is controlled by two parameters: the length scale γ_L, the ratio between the problem size and the interatomic equilibrium spacing, and the energy scale γ_E, relating the internal energy Π_{int} and the interaction energy Π_C. Further, in Section 5.4, we have applied our model to the interaction of CNTs. We have argued that, at both ends of the length scale spectrum, the CGCM reverts to either a MD model or to a macroscopic computational contact mechanics model.

There are several possible extensions to the theoretical and computational aspects of the work presented here, some of which are currently pursued by the authors. We have been able to obtain an excellent numerical agreement, see [26], of the CGCM with the Maugis–Dugdale model [15], an analytical adhesive contact model based on the JKR and DMT models [13, 14]. Another interesting

DOI: 10.1002/nme

topic is to study the formation and breaking of atomic bonds, which occur during sintering and fracture processes. The inclusion of frictional and thermal effects is also worth considering. Further computational topics are the consideration of surface smoothing in Method 3 and the scaling of the CGC Model as it approaches macroscale continuum mechanics [25].

ACKNOWLEDGEMENTS

This work is supported by a NSF grant (Grant No. CMS-0239130), which is greatly appreciated.

REFERENCES

1. Johnson KL. *Contact Mechanics*. Cambridge University Press: Cambridge, MA, 1985.
2. Laursen TA. *Computational Contact and Impact Mechanics*: *Fundamentals of Modelling Interfacial Phenomena in Nonlinear Finite Element Analysis*. Springer: Berlin, 2002.
3. Wriggers P. *Computational Contact Mechanics*. Wiley: Chichester, 2002.
4. Frenkel D, Smit B. *Understanding Molecular Simulation*: *From Algorithms to Applications* (2nd edn). Academic Press: San Diego, 2001.
5. Gao G, Çağin T, Goddard III WA. Energetics, structure, mechanical and vibrational properties of single-walled carbon nanotubes. *Nanotechnology* 1998; **9**:184–191.
6. Hertel T, Walkup RE, Avouris P. Deformation of carbon nanotubes by surface van der Waals forces. *Physical Review B* 1998; **58**(20):13870–13873.
7. Schlick T. *Molecular Modelling and Simulation*: *An Interdisciplinary Guide*. Springer: New York, 2002.
8. Fischer-Cripps AC. *Nanoindentation* (2nd edn). Springer: New York, 2004.
9. Sanz-Navarro CF, Kenny SD, Smith R. Atomistic simulations of structural transformations of silicon surfaces under nanoindentation. *Nanotechnology* 2004; **15**:692–697.
10. Saraev D, Miller RE. Atomistic simulation of nanoindentation into copper multilayers. *Modeling and Simulation in Materials Science and Engineering* 2005; **13**:1089–1099.
11. Binnig G, Quate CF, Gerber C. Atomic force microscope. *Physical Review Letters* 1986; **56**(9):930–933.
12. Cappella B, Dietler G. Force-distance curves by atomic force microscopy. *Surface Science Reports* 1999; **34**:1–104.
13. Johnson KL, Kendall K, Roberts AD. Surface energy and the contact of elastic solids. *Proceedings of the Royal Society of London*, *Series A* 1971; **324**:301–313.
14. Derjaguin BV, Muller VM, Toporov YP. Effect of contact deformation on the adhesion of particles. *Journal of Colloid and Interface Science* 1975; **53**(2):314–326.
15. Maugis D. Adhesion of spheres: the JKR–DMT transition using a dugdale model. *Journal of Colloid and Interface Science* 1992; **150**(1):243–269.
16. Tadmor EB, Ortiz M, Phillips R. Quasicontinuum analysis of defects in solids. *Philosophical Magazine A* 1996; **73**(6):1529–1563.
17. Knap J, Ortiz M. An analysis of the quasicontinuum method. *Journal of the Mechanics and Physics of Solids* 2001; **49**:1899–1923.
18. Bathe K-J. *Finite Element Procedures*. Prentice-Hall: Englewood Cliffs, NJ, 1996.
19. Belytschko T, Liu WK, Moran B. *Nonlinear Finite Elements for Continua and Structures*. Wiley: Chichester, 2000.
20. Qian D, Liu WK, Subramoney S, Ruoff RS. Effect of interlayer potential on mechanical deformation of multiwalled carbon nanotubes. *Journal of Nanoscience and Nanotechnology* 2003; **3**(1/2):185–191.
21. Israelachvili JN. *Intermolecular and Surface Forces* (2nd edn). Academic Press: London, 1991.
22. Miller RE, Tadmor EB. The quasicontinuum method: overview, applications and current directions. *Journal of Computer-Aided Material Design* 2002; **9**:203–239.
23. Hamaker HC. The London–Van der Waals attraction between spherical particles. *Physica* 1937; **4**(10):1058–1072.
24. Tadmor R. The London–van der Waals interaction energy between objects of various geometries. *Journal of Physical*: *Condensed Matter* 2001; **13**:L195–L202.
25. Sauer RA. An atomic interaction based continuum model for computational multiscale contact mechanics. *Ph.D. Thesis*, University of California, Berkeley, 2006.

DOI: 10.1002/nme

26. Sauer RA, Li S. An atomic interaction based continuum model for adhesive contact mechanics. *Finite Elements in Analysis and Design*, 2006.
27. Ogden RW. *Non-Linear Elastic Deformations*. Dover: Mineola, 1997.
28. Lucy LB. A numerical approach to the testing of the fission hypothesis. *The Astronomical Journal* 1977; **82**:1013–1024.
29. Gingold RA, Monaghan JJ. Smoothed particle hydrodynamics: theory and application to non-spherical stars. *Monthly Notices of the Royal Astronomical Society* 1977; **181**:375–389.
30. Goldhirsch I, Goldenberg C. On the microscopic foundations of elasticity. *European Physical Journal*, *Series E* 2002; **9**:245–251.
31. Bradley RS. The cohesive force between solid surfaces and the surface energy of solids. *Philosophical Magazine* 1932; **13**:853–862.
32. Arroyo M, Belytschko T. An atomistic-based finite deformation membrane for single layer crystaline films. *Journal of Mechanics and Physics of Solids* 2002; **50**:1941–1977.
33. Arroyo M, Belytschko T. Finite element methods for the non-linear mechanics of crystalline sheets and nanotubes. *International Journal for Numerical Methods in Engineering* 2004; **59**:419–456.
34. Rudd RE, Broughton JQ. Coarse-grained molecular dynamics: nonlinear finite elements and finite temperature. *Physical Review B* 2005; **72**:144104.
35. Girifalco LA, Hodak M, Lee RS. Carbon nanotubes, buckyballs, ropes, and a universal graphitic potential. *Physical Review B* 2000; **62**(19):13104–13110.
36. Zanzotto G. The Cauchy–Born hypothesis, nonlinear elasticity and mechanical twinning in crystals. *Acta Crystallographica*, *Section A* 1996; **52**:839–849.
37. Gao H, Klein P. Numerical simulation of crack growth in an isotropic solid with randomized internal cohesive bonds. *Journal of the Mechanics and Physics of Solids* 1998; **46**:187–218.
38. Friesecke G, Theil F. Validity and failure of the Cauchy–Born hypothesis in a two-dimensional mass-spring lattice. *Journal of Nonlinear Science* 2002; **12**:445–478.
39. Wu J-J. Adhesive contact between a nano-scale rigid sphere and an elastic half-space. *Journal of Physics D*: *Applied Physics* 2006; **39**:351–358.
40. Argento C, Jagoda A. Surface formulation for molecular interactions of macroscopic bodies. *Journal of the Mechanics and Physics of Solids* 1997; **45**(7):1161–1183.
41. Jagoda A, Argento C. An intersurface stress tensor. *Journal of Colloid and Interface Science* 1997; **191**:326–336.
42. Qian D, Wagner GJ, Liu WK, Yu M, Ruoff RS. Mechanics of carbon nanotubes. *Applied Mechanics Reviews* 2002; **55**(6):495–533.
43. Pantano A, Parks DM, Boyce MC. Mechanics of deformation of single- and multi-walled carbon nanotubes. *Journal of the Mechanics and Physics of Solids* 2004; **52**:789–821.
44. Reissner E. On one-dimensional finite-strain beam theory: the plane problem. *Journal of Applied Mathematical Physics* 1972; **23**:795–804.
45. Simo JC. A finite strain beam formulation. The three-dimensional dynamic problem. Part I. *Computer Methods in Applied Mechanics and Engineering* 1985; **49**:55–70.
46. Simo JC, Vu-Quoc L. A three-dimensional finite strain rod model. Part II: Computational aspects. *Computer Methods in Applied Mechanics and Engineering* 1986; **58**:79–116.
47. Hertel T, Martel R, Avouris P. Manipulation of individual carbon nanotubes and their interaction with surfaces. *Journal of Physical Chemistry*, *Series B* 1998; **102**(6):910–915.
48. Tang T, Jagoda A, Hui C-Y, Glassmaker NJ. Collapse of single-walled carbon nanotubes. *Journal of Applied Physics* 2005; **97**(7):074310.
49. Zhang S, Khare R, Belytschko T, Hsia KJ, Mielke SL, Schatz GC. Transition states and minimum energy pathways for the collapse of carbon nanotubes. *Physical Review B* 2006; **73**:075423.
50. Ruoff SR, Tersoff J, Lorents DC, Subramoney S, Chan B. Radial deformation of carbon nanotubes by van der Waals forces. *Nature* 1993; **364**:514–516.
51. Glassmaker NJ, Hui CY. Elastica solution for a nanotube formed by self-adhesion of a folded thin film. *Journal of Applied Physics* 2004; **96**(6):3429–3433.
52. Poncharal P, Wang ZL, Ugarte D, de Heer WA. Electrostatic deflections and electromechanical resonances of carbon nanotubes. *Science* 1999; **283**:1513–1516.
53. Qian D, Wagner GJ, Liu WK. A multiscale projection method for the analysis of carbon nanotubes. *Computer Methods in Applied Mechanics and Engineering* 2004; **193**:1603–1632.

DOI: 10.1002/nme